$D\bar{D}$ interactions are weak near threshold in QCD

David J. Wilson,[1,*] Jozef J. Dudek,[2,†] Robert G. Edwards,[3,‡] and Christopher E. Thomas[1,§]

(For the Hadron Spectrum Collaboration)

[1]*DAMTP, University of Cambridge, Centre for Mathematical Sciences, Wilberforce Road, Cambridge CB3 0WA, United Kingdom*
[2]*Department of Physics, College of William and Mary, Williamsburg, Virginia 23187, USA*
[3]*Thomas Jefferson National Accelerator Facility, 12000 Jefferson Avenue, Newport News, Virginia 23606, USA*

(Received 9 March 2026; accepted 15 July 2026; published 14 September 2026)

We study near-threshold $D\bar{D}$ scattering in S- and D-wave to determine whether or not resonances or bound states are present. Working in the approximation where charm annihilation is forbidden, with two degenerate light-quark flavors and a heavier strange quark, isospin is a good quantum number, and the only other channel that is kinematically open is $\eta_c\eta$. Using lattice QCD we compute, as a function of varying light-quark mass, the S-matrix for coupled-channel $\eta_c\eta - D\bar{D}$ scattering and find only weakly interacting meson pairs. In contrast to several other studies, we find no evidence for any bound-state or resonance singularity in the energy region between the deeply bound $\chi_{c0}(1P)$ state and the $D_s\bar{D}_s$ threshold.

DOI: 10.1103/s3p2-552r

I. INTRODUCTION

Many apparently straightforward questions regarding what quantum chromodynamics (QCD) predicts for hadron-hadron scattering amplitudes remain unanswered. Such amplitudes may feature short-lived resonances above threshold or bound states below threshold, potentially giving rise to enhancements in experimental production of the corresponding hadron-hadron pair. Of particular interest to the current generation of experiments exploring the spectrum of excited hadrons are processes involving charm quarks. These are readily observed at LHCb, Belle-II, and BES-III, among others, where pairs of open-charm hadrons are formed in a variety of ways. From both experimental and theoretical standpoints, the behavior of one of the simplest systems, near-threshold $D\bar{D}$ scattering (in isospin-0) in S-wave, remains unclear.

Lying well below the $D\bar{D}$ threshold, the $\chi_{c0}(3415)$, which has only $c\bar{c}$ annihilation decays in QCD, is readily interpreted as something closely resembling a quark model $c\bar{c}(1P)$ state. Above this, the situation becomes much less clear. Quark model expectations are for $c\bar{c}(2P)$ states above 3900 MeV, which would suggest a single χ'_{c0} resonance well above $D\bar{D}$ threshold, with then a significant gap before the next quark model state. In contrast to such a simple picture, experimentally there are claims for as many as four resonance states above the $\chi_{c0}(3415)$ and below 4 GeV, each appearing in either a single final state ($J/\psi\omega$ [1], $D\bar{D}$ [2,3], $D_s\bar{D}_s$ [4]) or a single production process, $e^+e^- \to J/\psi D\bar{D}$ [5].

Theoretically, approaches which consider strong interactions between heavy mesons suggest attraction or even binding into *meson-meson molecules* is possible [6,7], usually via pseudoscalar or vector meson exchange. Significant effects are predicted near many meson-meson S-wave thresholds [7]. Approaches based on a diquark-antidiquark color attraction, leading to compact *tetraquarks*, suggest many states beyond the usual quark model counting, including with J^{PC} quantum numbers other than those accessible to a meson-meson pair in S-wave [8,9]. Approaches considering both meson-meson and quark-antiquark degrees of freedom suggest a wide range of possible mixing between these components [10–13].

One difficulty in building an interpretation of the experimental spectrum, is that none of the currently explored experimental processes that ultimately produce $D\bar{D}$ pairs are completely straightforward to analyze. Some have a complex progenitor such as a heavy B-meson decaying through a

*Contact author: d.j.wilson@damtp.cam.ac.uk
†Contact author: jjdudek@wm.edu
‡Contact author: edwards@jlab.org
§Contact author: c.e.thomas@damtp.cam.ac.uk

Published by the American Physical Society under the terms of the Creative Commons Attribution 4.0 International license. Further distribution of this work must maintain attribution to the author(s) and the published article's title, journal citation, and DOI. Funded by SCOAP³.

three-hadron process, where interactions with the third hadron can have a nontrivial impact. Another possibility is production via two-photon fusion [14,15], and here the Born diagram with a t-channel D exchange has the possibility to significantly distort the energy dependence near $D\bar{D}$ threshold relative to the $D\bar{D}$ elastic scattering amplitude [16,17]. Such distortion is well known in the $\gamma\gamma \to \pi\pi$ and $\gamma\gamma \to K\bar{K}$ processes, which bear little resemblance to the S-wave s-channel $\pi\pi \to \pi\pi$ and $\pi\pi \to K\bar{K}$ processes [18–20].

In the past 20 years, many of the new resonances claimed experimentally have been observed close to S-wave hadron-hadron thresholds. In order to answer questions about whether or not this is accidental, or a hint at an important poorly understood dynamical aspect of QCD, we must obtain clean first-principles predictions from the underlying theory of QCD.

Lattice QCD offers the opportunity to do just this, making only controlled approximations to QCD, such as the use of a lattice spacing cutoff which can ultimately be removed. Use of a finite spatial volume means the theory has a discrete spectrum, and this spectrum can be used to constrain hadron-hadron scattering amplitudes [21–23]. The theory can be studied as a function of quark mass, exploring the sensitivity of observables to these parameters whose particular values are external to QCD.

A detailed lattice QCD study using light quarks with mass such that $m_\pi \sim 391$ MeV was reported in Refs. [24,25]. Analyzing finite-volume spectra up to the $J/\psi\phi$ threshold, coupled-channel amplitudes describing all relevant kinematically open channels were determined, and in these no near-threshold resonances or bound states were found. The only S-wave singularity required was found to be a quark–model-like state appearing above the $D_s\bar{D}_s$ threshold.[1]

The result of Refs. [24,25] was in stark contrast to an earlier lattice QCD calculation, presented in Ref. [27], using 280 MeV pions, which concluded that all of the following were required in order to describe its finite-volume spectrum: a stable bound-state 4 MeV below $D\bar{D}$ threshold, an extremely narrow resonance on top of the $D_s\bar{D}_s$ threshold, and another broader resonance above $D\bar{D}$ threshold.[2]

While unlikely, it remained possible that these two calculations were in fact compatible, through the $D\bar{D}$ scattering process having an unexpectedly strong dependence upon the light-quark mass. It is to this possibility that we turn in this paper, by considering the techniques of Refs. [24,25] at three lighter pion masses, $m_\pi \sim 239$, 283 and 330 MeV. We find that, contrary to the observations presented in Ref. [27], there appear to be no significant finite-volume energy shifts in levels near to the $D\bar{D}$ threshold, and that the resulting scattering amplitudes feature no nearby singularities corresponding to bound-states or resonances.[3]

II. LATTICE QCD SETUP

Our calculational approach follows that of Ref. [25], where details can be found. In this paper we report on the use of three different light quark mass choices using lattices whose properties are summarized in Table I. These are anisotropic lattices with $N_f = 2 + 1$ flavors of dynamical quarks, with the action described in Refs. [29,30]. The valence charm quarks use the same Wilson-clover action as the light and strange quarks. The lattice scale is determined by setting the computed Ω baryon mass to its physical value, such that each lattice has spacing close to $a_t \sim 0.033$ fm temporally and $a_s \sim 0.12$ fm spatially. The charm quark is tuned by adjusting the bare charm quark mass parameter on each lattice such that the η_c mass is close to its physical value [31,32].

A large basis of operators includes single-meson-like constructions formed from gamma matrices and up to three gauge covariant derivatives [33] and meson-meson-like constructions formed from product pairs of optimized single-meson-like constructions [34,35]. Quark fields are smeared with *distillation* [36] with the number of Laplacian eigenvectors given in Table I. $c\bar{c}$ annihilation is forbidden by excluding Wick contractions in which it occurs, but light and strange annihilation is included without further approximation. Discrete spectra follow from diagonalizing a computed matrix of correlation functions, solving a generalized eigenvalue problem [37,38]. Fits to the time dependence of the eigenvalues are performed over various time windows, and the energies used correspond to a weighted average over many such fits (see Appendix E of Ref. [39]).

Our basis of operators includes constructions resembling $\eta_c\eta$, $D\bar{D}$, $D_s\bar{D}_s$, $\eta_c\eta'$, and $\psi\omega$. The thresholds for the last three of these lie above the $\eta_c\eta - D\bar{D}$ scattering region that is our main focus in this study. Including higher-lying operators helps to give us confidence in the extracted spectrum. In practice we find that excluding $\eta_c\eta'$ operators altogether leaves the spectrum below $D_s\bar{D}_s$ threshold unchanged.[4] Stable hadron masses and hadron-hadron channel thresholds

[1]The PDG [26] currently combines the narrow resonances observed experimentally in $J/\psi\omega$, $D\bar{D}$ and $D_s\bar{D}_s$ into a single entry, the $\chi_{c0}(3915)$. The only additional experimental scalar candidate in this energy region is the broad $\chi_{c0}(3860)$ claimed in $e^+e^- \to J/\psi D\bar{D}$, but not required in descriptions of $B \to KD\bar{D}$.

[2]While the analysis of Ref. [27] used piecewise amplitudes whose analyticity could be questioned, reanalysis of the energy levels of Ref. [27] using more consistent amplitudes led to a comparable state content [28], although the quality of fit of the finite-volume spectrum description is poor.

[3]While in this calculation we do not determine amplitudes to higher energies (e.g., above the $D_s\bar{D}_s$ threshold), we expect the picture observed in Refs. [24,25] to continue to hold, with a single narrow resonance comparable to the $\chi_{c0}(3915)$.

[4]As in Ref. [25], correlators featuring $\eta_c\eta'$ operators are found to be noisy and when included, the indications are for an approximate decoupling of the related channel.

TABLE I. Details of the $N_f = 2 + 1$ anisotropic lattices used in this study corresponding to the actions described in Refs. [29,30]. Results on the lattices in the bottom row were presented previously in Refs. [24,25]. N_{cfgs} is the number of gauge configurations used, N_{vecs} is the number of vectors used in the distillation approach, and $N_{\text{t}_{\text{src}}}$ is the number of time sources averaged in computing the correlation matrix.

$-a_t m_\ell$	$(L/a_s)^3 \times T/a_t$	N_{cfgs}	N_{vecs}	$N_{\text{t}_{\text{src}}}$	$a_t m_\pi$	$a_t m_\Omega$	ξ_π	m_π/MeV
0.0860	$32^3 \times 256$	485	384	2–4	0.03928(18)	0.2751(6)	3.453(6)	239
0.0856	$\{24^3, 32^3\} \times 256$	$\{400, 481\}$	$\{160, 256\}$	4–8	0.04720(11)	0.2793(8)	3.457(6)	283
0.0850	$24^3 \times 256$	481	160	4–8	0.05635(14)	0.2857(8)	3.456(9)	330
0.0840	$\{16^3, 24^3\} \times 128$	$\{478, 553\}$	$\{64, 160\}$	*2–8*	*0.06906(13)*	*0.2951(22)*	*3.444(6)*	*391*
	$20^3 \times 256$	288	128					

TABLE II. Top: Stable hadron masses in temporal lattice units, $a_t m$. Bottom: Two, three and four hadron thresholds in temporal lattice units.

	239 MeV	283 MeV	330 MeV
π	0.03928(18)	0.04720(11)	0.05635(14)
K	0.08344(7)	0.08659(14)	0.09027(15)
η	0.09299(56)	0.09427(70)	0.09790(100)
η'	0.15666(200)	0.16052(140)	0.16286(156)
ω	0.13616(107)	0.14081(61)	0.14710(86)
D	0.30923(11)	0.31406(11)	0.32255(11)
D_s	0.32356(12)	0.32785(6)	0.33548(8)
D^*	0.33058(24)	0.33572(16)	0.34408(16)
D_s^*	0.34448(15)	0.34877(8)	0.35641(12)
η_c	0.49097(4)	0.49773(3)	0.50973(4)
J/ψ	0.50553(5)	0.51218(3)	0.52391(5)

	239 MeV	283 MeV	330 MeV
$\eta_c\eta$	0.5840(6)	0.5920(7)	0.6076(10)
$D\bar{D}$	0.6185(2)	0.6281(2)	0.6451(2)
$D\bar{D}^*$	0.6398(3)	0.6498(2)	0.6666(2)
$\psi\omega$	0.6417(11)	0.6530(6)	0.6710(9)
$D_s\bar{D}_s$	0.6471(2)	0.6557(1)	0.6710(1)
$\eta_c\eta'$	0.6476(20)	0.6583(14)	0.6726(16)
$D^*\bar{D}^*$	0.6612(3)	0.6714(2)	0.6882(2)
$\eta_c\pi\pi$	0.5695(3)	0.5921(2)	0.6224(2)
$J/\psi\pi\pi\pi$	0.6234(3)	0.6538(2)	0.6930(2)
$\chi_{c0}\pi\pi$	0.6463(3)	0.6697(4)	0.7015(3)
$D\bar{D}\pi$	0.6577(2)	0.6753(2)	0.7015(2)

for the three different light quark masses are presented in Table II. We also list some three- and four-hadron channels that can in principle contribute, but in each case we expect them to be highly suppressed either by large required values of ℓ or by their high-lying thresholds.[5]

The relevant symmetries of the periodic cubic volume are reflected in the use of cubic group irreducible representations (irreps), with a detailed description for the current case given in Ref. [25]. In this study we compute only a limited set of irreps, $[000]A_1^+$, $[001]A_1$ and $[000]E^+$, that we find is able to provide enough constraint to determine S-wave and D-wave scattering in the energy region of interest. Due to the modest energy range considered, the basis of operators used (Appendix A) is a relatively small subset of those used in Ref. [25], which considered amplitudes to a much higher energy.

TABLE III. Anisotropies determined for the π, η, D, and η_c mesons. Values for $m_\pi \sim 239$ MeV taken from Refs. [40,41]. The final row indicates the estimate used in the scattering analyses in this study, whose central value comes from the pion determination with an error inflated to account for the variation above.

	239 MeV	283 MeV	330 MeV
ξ_π	3.453(6)	3.457(6)	3.456(9)
ξ_η	3.468(20)	3.408(10)	3.438(9)
ξ_D	3.443(7)	3.432(4)	3.448(6)
ξ_{η_c}	3.456(4)	3.457(2)	3.477(2)
ξ	3.453(17)	3.457(25)	3.456(14)

Independent determination of the energy of stable hadrons at various values of three-momentum leads to a measure of the dispersion relation from which an estimate of the lattice anisotropy, $\xi = a_s/a_t$, can be extracted. While each hadron is found to obey the relativistic dispersion relation to an excellent approximation, the values of the anisotropy extracted exhibit a modest scatter across different hadrons. We choose to propagate a systematic uncertainty due to that variation through the determination of the scattering amplitudes. Since we focus in this paper mainly on *near-threshold* $D\bar{D}$ scattering, in practice we find relatively little sensitivity to this conservative approach. Table III presents the determined ξ values for relevant stable hadrons, and the value for each pion mass (with inflated error) to be used later.

We also add an additional uncertainty ($a_t \delta E_{\text{syst}} = 0.00050$) to every energy level determined on the $m_\pi \sim 283$ MeV lattices to account for slight differences in the η_c and D-meson masses when determined individually on these

[5]We do not include any operators resembling three-hadron channels, such as $\chi_{c0}\pi\pi$ or $D\bar{D}\pi$.

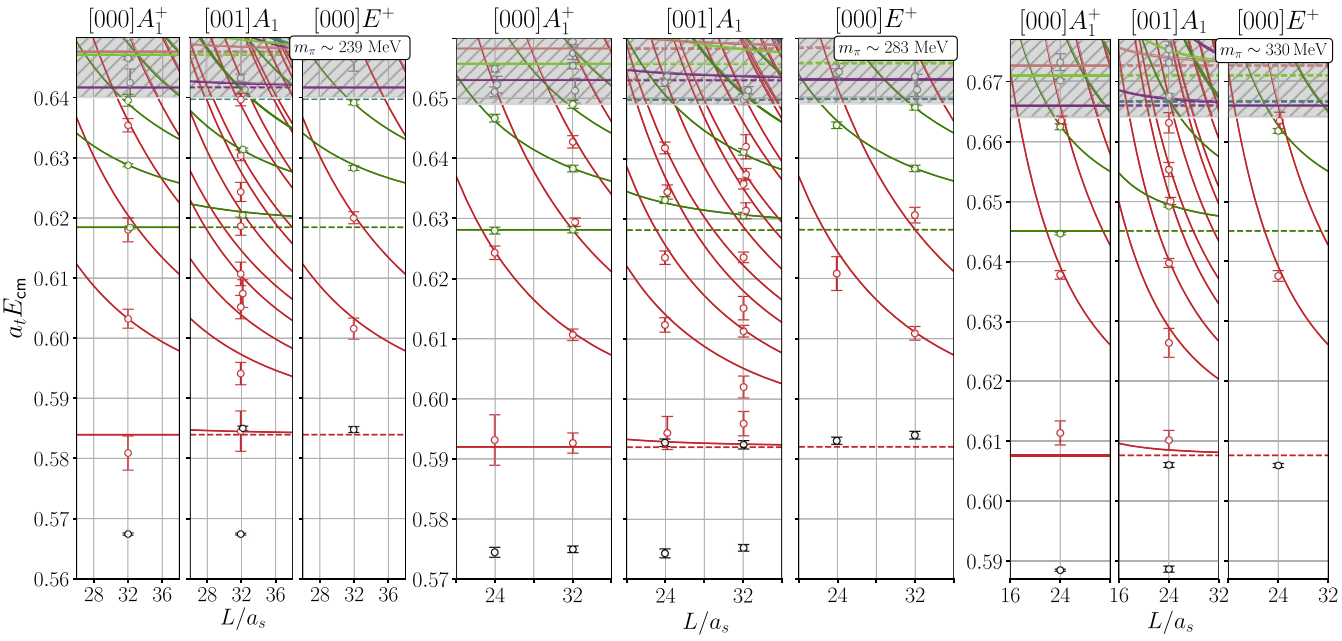


FIG. 1. Finite-volume spectra in three irreps determined on the lattices described in Sec. II. Energy levels are colored according to their dominant operator overlap determined in the diagonalization of the matrix of correlation functions: $\eta_c\eta$-like (red), $D\bar{D}$-like (green), $c\bar{c}$-like (black). Gray points in the hatched high-energy region are not used in the subsequent determination of scattering amplitudes. Curves indicate the noninteracting spectrum of meson pairs on the relevant volumes with the same color coding, with the addition of $\psi\omega$ (purple) and $D_s\bar{D}_s$ (light green) appearing above the energy cutoff. Dashed lines show the relevant meson-meson kinematic thresholds.

two volumes, following the approach described in Refs. [24,25].

III. FINITE VOLUME SPECTRA

Figure 1 shows the discrete spectra of finite-volume energy levels on each of the lattices described in the previous section across three irreps. The $[000]A_1^+$ irrep at low energies will be dominated by S-wave scattering, while $[000]E^+$ has its dominant contribution from D-wave scattering. $[001]A_1$ receives contributions from both S-wave and D-wave. As well as the finite-volume spectrum extracted from computed matrices of correlation functions, we also show the spectrum of *noninteracting* meson pair energies in finite volume, computed according to

$$a_t E_{\mathrm{lat}} = \left[(a_t m_1)^2 + \left(\frac{2\pi}{\xi L/a_s}\right)^2 |\mathbf{n}_1|^2\right]^{1/2} + \left[(a_t m_2)^2 + \left(\frac{2\pi}{\xi L/a_s}\right)^2 |\mathbf{n}_2|^2\right]^{1/2},$$

$$a_t E_{\mathrm{cm}} = \left[(a_t E_{\mathrm{lat}})^2 - \left(\frac{2\pi}{\xi L/a_s}\right)^2 |\mathbf{n}_2 + \mathbf{n}_1|^2\right]^{1/2},$$

where $\mathbf{n}_{1,2}$ are the discrete (integer triplet) momenta of the mesons which sum to the total momentum in the irrep characterization (see Refs. [24,25] for more details appropriate to the current case).

The single low-lying energy level observed in $[000]A_1^+$, also seen as the lowest level in $[001]A_1$, is interpreted as being due to the stable $\chi_{c0}(1P)$, while the lowest energy level in $[000]E^+$, seen also in $[001]A_1$, is the stable $\chi_{c2}(1P)$. Above these we observe energy levels which are found to have dominant overlap onto either $\eta_c\eta$-like (red) or $D\bar{D}$-like (green) operators, all lying very close to noninteracting energies.

The pattern of operator overlaps suggests limited channel coupling between $\eta_c\eta$ and $D\bar{D}$ scattering channels, and the fact that the $D\bar{D}$-like states show no systematic departures from the $D\bar{D}$ noninteracting energies, leads us to anticipate only very weak, effectively decoupled, $D\bar{D}$ scattering at all three pion masses, and does not suggest the presence of any bound states or resonances near to the $D\bar{D}$ threshold.

In the previous calculation with $m_\pi \sim 391$ MeV, reported on in Refs. [24,25], the spectrum was determined with a larger basis of operators allowing higher-lying levels to be reliably extracted. Within this extended spectrum, departures from noninteracting energies were observed higher in the spectrum, together with an "extra" level lying above the $D_s\bar{D}_s$ threshold, characteristic of a narrow resonance, as was found when the finite-volume spectrum was described by scattering amplitudes.

IV. SCATTERING AMPLITUDES

Much theoretical focus has been on the behavior of $D\bar{D}$ scattering in S-wave at kinematical threshold, but it is

important to realize that this does not correspond to *elastic* scattering, even in the approximation that charm-anticharm quark pairs are forbidden to annihilate. With the same quantum numbers, the two-hadron channel $\eta_c\eta$ is kinematically accessible. Some motivation for neglecting this channel comes from the longstanding empirically motivated Okubo-Zweig-Iizuka rule [42–44] in which coupling of charmonia to *open-charm* channels, like $D\bar{D}$, is expected to dominate over coupling to *hidden-charm* channels, like $\eta_c\eta$, when both are kinematically open.

We wish to study this system in first-principles in QCD, so we will not make any unjustified assumptions about the relative importance of any particular open channel. Indeed, the Lüscher approach, presented below, which relates scattering amplitudes to finite-volume spectra, requires us to consider all kinematically open scattering channels in the energy region of interest. In the current case, for all three pion masses considered, the $\eta_c\eta$ channel opens well below the $D\bar{D}$ channel, with the next channels able to contribute to S-wave scattering, $\psi\omega$ and $D_s\bar{D}_s$, opening at higher energy. Our intent then is to determine coupled-channel $\eta_c\eta - D\bar{D}$ S-wave amplitudes constrained by the finite-volume spectra presented in the previous section. From these amplitudes we will examine whether the channels are close to being decoupled, and whether there are strong interactions near the $D\bar{D}$ threshold which can be explained in terms of bound states or resonances.

The relevant relationship between scattering amplitudes and finite-volume spectra [21,45,46], sometimes referred to as the *Lüscher quantization condition*, can be written as

$$\det\left[\mathbf{1} + i\boldsymbol{\rho}(E)\cdot\boldsymbol{t}(E)\cdot(\mathbf{1} + i\boldsymbol{\mathcal{M}}(E,L))\right] = 0, \qquad (1)$$

where $\boldsymbol{\rho}$ is a diagonal matrix of phase-space factors $\rho_{ij} = (2k_i/\sqrt{s})\delta_{ij}$, k_i is the cm momentum of the meson-meson pair in channel i, and $\boldsymbol{t}(E)$ is the scattering t-matrix. The kinematical matrix $\boldsymbol{\mathcal{M}}$ encapsulates the volume and irrep dependence in a known manner. Those energies where the determinant vanishes correspond to the spectrum, $E_{\mathfrak{n}}(L)$, in an $L\times L\times L$ periodic volume for a particular scattering amplitude $\boldsymbol{t}(E)$.

Practical use of this equation to constrain coupled-channel scattering requires parametrization of the t-matrix, and this can be achieved in a manner that respects s-channel unitarity using the K-matrix,

$$\boldsymbol{t}^{-1} = \boldsymbol{K}^{-1} + \boldsymbol{I},$$

where $\mathrm{Im}\,\boldsymbol{I} = -\boldsymbol{\rho}$ above threshold. A real part for $\boldsymbol{I}$ can be generated from a dispersion relation if desired to improve somewhat the analytical properties of the t-matrix. For our purposes we will make use of the following simple parametrizations of the K-matrix:

$$K_{ij} = (2k_i)^{\ell_i}\hat{K}_{ij}(2k_j)^{\ell_j},$$
$$\hat{K}_{ij} = \frac{g_i g_j}{m^2 - s} + \gamma_{ij}^{(0)} + \gamma_{ij}^{(1)}\cdot\frac{s - 4m_D^2}{4m_D^2}. \qquad (2)$$

The factors $(2k_i)^{\ell_i}$ are introduced to encourage the correct behavior at threshold for a partial wave with angular momentum ℓ. Inclusion of a pole term in the parametrization allows for efficient description of a nearby bound state or resonance, but in practice we will find that its only use in this calculation is to (optionally) describe the deeply bound $\chi_{c0}(1P)$ and $\chi_{c2}(1P)$ states.

Reference [47] discusses the finite-volume approach in more detail, and Ref. [48] provides an efficient technique to solve Eq. (1) in the coupled-channel case. As discussed in Refs. [24,25], the data correlation matrix characterizing the computed discrete energy levels can be rendered better conditioned by resetting a modest number of small singular values in computation of its inverse.

We will illustrate our analysis using the $m_\pi \sim 283$ MeV lattice, on which we have the greatest degree of constraint, before discussing the two other pion masses, where the results are qualitatively similar.

A. $m_\pi \sim 283$ MeV

As shown in Fig. 1 (central panels), across two lattice volumes there are 42 energy levels which can be used to constrain coupled-channel $\eta_c\eta - D\bar{D}$ scattering in S-wave and D-wave below our choice of cutoff at $a_t E_{\mathsf{cm}} \sim 0.65$, lying somewhat below the $\psi\omega$ and $D_s\bar{D}_s$ thresholds. Eight of these levels (colored black in the figure) can be identified as being due to the stable $\chi_{c0}(1P)$ and $\chi_{c2}(1P)$ states, and in a first approximation these subthreshold bound states can be assumed to have negligible impact upon the scattering system at higher energies. As such we will initially not attempt to describe them, and later we will relax this assumption, finding it to be very well justified.

We find that the remaining 34 energy levels can be described quite well by a *constant* K-matrix for each of S-wave and D-wave, together with the dispersively improved Chew-Mandelstam phase space[6] subtracted at the threshold energy for each channel,

[6]Our implementation is described in Ref. [49].

$$\begin{aligned}
\gamma^{(S)}_{\eta_c\eta,\eta_c\eta} &= (-0.09 \pm 0.20 \pm 0.39) \\
\gamma^{(S)}_{\eta_c\eta,D\bar{D}} &= (0.00 \pm 0.12 \pm 0.19) \\
\gamma^{(S)}_{D\bar{D},D\bar{D}} &= (0.66 \pm 0.27 \pm 0.35) \\
\gamma^{(D)}_{\eta_c\eta,\eta_c\eta}/a_t^4 &= (1.0 \pm 0.5 \pm 1.3) \times 10^3 \\
\gamma^{(D)}_{\eta_c\eta,D\bar{D}}/a_t^4 &= (0.00 \pm 0.97 \pm 0.48) \times 10^3 \\
\gamma^{(D)}_{D\bar{D},D\bar{D}}/a_t^4 &= (0.48 \pm 0.29 \pm 0.34) \times 10^3
\end{aligned}
\begin{bmatrix}
1 & 0.39 & 0.15 & -0.05 & -0.01 & 0.07 \\
 & 1 & 0.01 & -0.03 & -0.04 & 0.03 \\
 & & 1 & 0.02 & -0.00 & 0.11 \\
 & & & 1 & 0.00 & -0.09 \\
 & & & & 1 & -0.01 \\
 & & & & & 1
\end{bmatrix} \tag{3}$$

$$\chi^2/N_{\mathrm{dof}} = \tfrac{35.4}{34-6-3} = 1.41.$$

For each parameter, the first quoted uncertainty comes from the standard consideration of the curvature of the χ^2 minimum, while the second reflects variation under adjustments of the scattering hadron masses and the anisotropy to their $\pm 1\sigma$ values. The correlations between parameters determined at the minimum are shown in the matrix on the right. The superscripts in circular brackets indicate the angular momentum ℓ. The reduced χ^2 includes a subtraction of 3 degrees of freedom from three reset singular values in the computation of the inverse of the data correlation matrix.[7] Channel-coupling parameters are clearly being driven to zero value in this fit, and indeed forcing them to be exactly zero yields a slightly reduced value of $\chi^2/N_{\mathrm{dof}} = \frac{35.4}{34-4-3} = 1.31$. The remaining parameters, effectively describing *decoupled* $\eta_c\eta - D\bar{D}$ scattering in S-wave and D-wave, are observed to be broadly compatible with zero, suggesting only weak scattering in each of these channels in the energy region constrained by our discrete energy levels.

This amplitude description is shown in Fig. 2 (left panel) where we observe explicitly the weak decoupled scattering in both $\eta_c\eta$ and $D\bar{D}$ channels. The bottom panel illustrates the good global description of the finite-volume spectrum provided by this amplitude, excluding the deeply bound $\chi_{c0}(1P)$ and $\chi_{c2}(1P)$ states that we did not attempt to describe.

The S-wave amplitude of Eq. (3) has no nearby pole singularities on any of the four Riemann sheets of coupled-channel $\eta_c\eta - D\bar{D}$ scattering, as we would expect given the observed weakness of interaction.

Although we obtained an excellent description of the finite-volume spectrum above using a *constant* K-matrix, we can also consider introducing more energy dependence into the parametrization. In this case we choose to enforce $\eta_c\eta$, $D\bar{D}$ decoupling by setting off diagonal elements of the K-matrix to zero, but we allow the S-wave $D\bar{D}$ K-matrix element to have a term in Eq. (2) with nonzero $\gamma^{(1)}$, i.e., allowing behavior linear in s, giving a fit description,

$$\begin{aligned}
\gamma^{(0)(S)}_{\eta_c\eta,\eta_c\eta} &= (-0.09 \pm 0.09 \pm 0.49) \\
\gamma^{(0)(S)}_{D\bar{D},D\bar{D}} &= (-0.67 \pm 0.84 \pm 2.73) \\
\gamma^{(1)(S)}_{D\bar{D},D\bar{D}} &= (0.2 \pm 12.8 \pm 6.1) \\
\gamma^{(0)(D)}_{\eta_c\eta,\eta_c\eta}/a_t^4 &= (1.0 \pm 0.5 \pm 1.3) \times 10^3 \\
\gamma^{(0)(D)}_{D\bar{D},D\bar{D}}/a_t^4 &= (0.47 \pm 0.32 \pm 0.32) \times 10^3
\end{aligned}
\begin{bmatrix}
1 & 0.14 & -0.12 & 0.01 & 0.08 \\
 & 1 & -0.95 & 0.22 & 0.42 \\
 & & 1 & -0.23 & -0.42 \\
 & & & 1 & 0.01 \\
 & & & & 1
\end{bmatrix} \tag{4}$$

$$\chi^2/N_{\mathrm{dof}} = \tfrac{35.4}{34-5-3} = 1.36.$$

We observe that the fit quality is essentially the same as the previous parametrization, with the coefficient of the term linear in s being compatible with zero, and also significantly anticorrelated with the corresponding constant term. The resulting amplitudes show no systematic differences from those plotted in Fig. 2 (left panel).

We can return to the question of whether the presence of the deeply bound stable $\chi_{c0}(1P)$ and $\chi_{c2}(1P)$ states has any relevant impact for the scattering amplitudes above $\eta_c\eta$ threshold. Including the relevant finite-volume energy levels into our constraint, and adding a pole term in each of the S-wave and the D-wave K-matrix parametrizations, we can find a description,

[7]Retaining the full inverse data correlation matrix leads to extremely similar parameter values and a similar fit quality, $\chi^2/N_{\mathrm{dof}} = \frac{46.8}{34-4} = 1.56$.

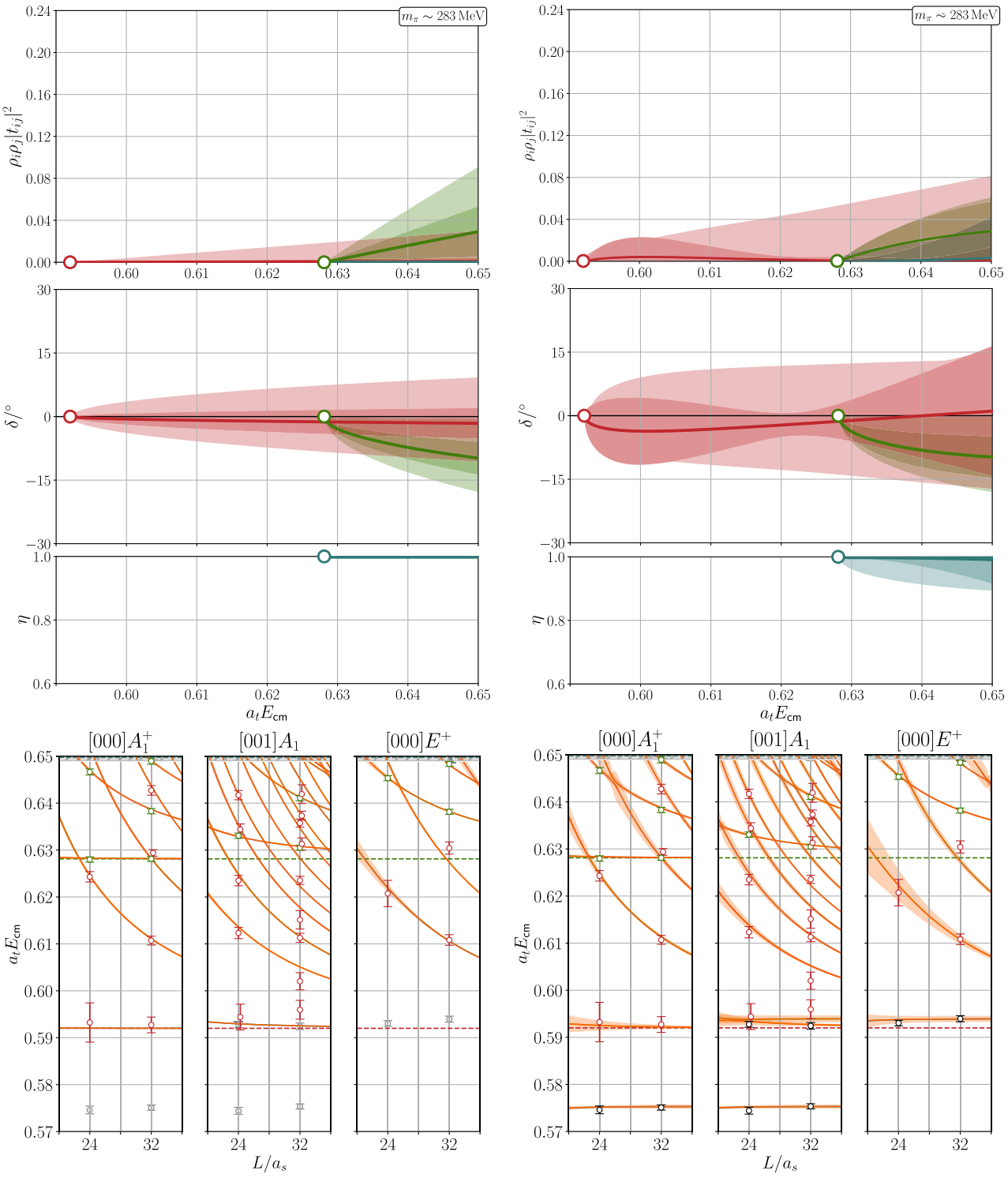


FIG. 2. Coupled $\eta_c\eta - D\bar{D}$ S-wave scattering amplitude descriptions of finite-volume spectra. Left: amplitudes of Eq. (3). Right: amplitudes of Eq. (5). Top panels illustrate the magnitude with a normalization where the unitarity limit is 1 for $t_{\eta_c\eta,\eta_c\eta}$ (red) and $t_{D\bar{D},D\bar{D}}$ (green). Center panels show channel phase shifts, $\delta_{\eta_c\eta}$ (red), $\delta_{D\bar{D}}$ (green) and inelasticity, η, defined so that the diagonal elements of the 2×2 t-matrix are $t_{ii} = \frac{\eta e^{2i\delta_i}-1}{2i\rho_i}$ and the off diagonal element is $t_{ij} = \frac{\sqrt{1-\eta^2}e^{i(\delta_i+\delta_j)}}{2\sqrt{\rho_i\rho_j}}$. Bottom panels show the finite-volume spectrum given by the amplitude (orange curves) compared with the spectrum constraining the amplitudes.

$$
\begin{aligned}
a_t m^{(S)} &= (0.57528 \pm 0.00041 \pm 0.00002) \\
a_t g^{(S)}_{\eta_c\eta} &= (0.17 \pm 0.25 \pm 0.29) \\
a_t g^{(S)}_{D\bar{D}} &= (-0.28 \pm 0.10 \pm 0.10) \\
\gamma^{(S)}_{\eta_c\eta,\eta_c\eta} &= (0.4 \pm 1.5 \pm 0.0) \\
\gamma^{(S)}_{\eta_c\eta,D\bar{D}} &= (-0.7 \pm 2.5 \pm 0.0) \\
a_t m^{(D)} &= (0.59392 \pm 0.00072 \pm 0.00000) \\
g^{(D)}_{\eta_c\eta}/a_t &= (4 \pm 9 \pm 55)^{(\dagger)} \\
\gamma^{(D)}_{\eta_c\eta,\eta_c\eta}/a_t^4 &= (1.3 \pm 0.5 \pm 1.5) \times 10^3 \\
\gamma^{(D)}_{D\bar{D},D\bar{D}}/a_t^4 &= (0.37 \pm 0.26 \pm 0.28) \times 10^3
\end{aligned}
\quad
\begin{bmatrix}
1 & 0.70 & -0.62 & 0.70 & -0.70 & 0.66 & 0.07 & -0.05 & -0.39 \\
 & 1 & -0.81 & 0.99 & -1.00 & 0.94 & 0.10 & -0.05 & -0.50 \\
 & & 1 & -0.79 & 0.84 & -0.78 & -0.08 & 0.05 & 0.46 \\
 & & & 1 & -0.99 & 0.92 & 0.10 & -0.06 & -0.49 \\
 & & & & 1 & -0.93 & -0.10 & 0.05 & 0.50 \\
 & & & & & 1 & 0.05 & -0.04 & -0.47 \\
 & & & & & & 1 & -0.15 & -0.05 \\
 & & & & & & & 1 & -0.05 \\
 & & & & & & & & 1
\end{bmatrix}
$$

$$\chi^2/N_{\mathrm{dof}} = \tfrac{32.1}{42-9-4} = 1.11. \tag{5}$$

Any parameter in Eq. (2) not specified above is fixed to zero in this description, and Chew-Mandelstam phase space is used, this time subtracted at the locations of the pole parameters $m^{(\ell)}$. Any effect above threshold from the presence of a D-wave pole below threshold is heavily suppressed by the centrifugal barrier such that it proves necessary to *force* there to be a nonzero coupling to the $\eta_c\eta$ channel to ensure a solution to Eq. (1) near the location of the $\chi_{c2}(1P)$ state. This is indicated by the $^{(\dagger)}$ above, where this parameter was limited in the χ^2 minimization such that $|g^{(D)}_{\eta_c\eta}|/a_t \geq 4$. Using smaller magnitudes of this coupling cutoff, or forcing a nonzero coupling to $D\bar{D}$ instead, were also explored, with only tiny changes to the fit quality.

We observe that there are two well-determined K-matrix pole mass parameters in Eq. (5), whose numerical values closely correspond with the location of the low-lying previously excluded energy levels in Fig. 1. As seen in Fig. 2 (right panel), the additional finite-volume energy levels below threshold are well described by this amplitude.

This description of the finite-volume spectrum can be seen in Fig. 2 (right panel) to again correspond to weak scattering above threshold for both $\eta_c\eta$ and $D\bar{D}$, with no significant difference in behavior observed relative to the description ignoring the presence of the deeply bound states.

The amplitude in Eq. (5), as expected, has an S-wave t-matrix pole at $a_t\sqrt{s} = 0.57528(40)$ corresponding to the bound state $\chi_{c0}(1P)$. In addition there are further poles located either on sheets not close to physical scattering, or distant in the complex energy plane, none of which have a significant influence on scattering above threshold.

The only relevant t-matrix pole in D-wave is found at $a_t\sqrt{s} = 0.59392(76) - \frac{i}{2}0.00002(11)$ on the Im $k_{\eta_c\eta} < 0$, Im $k_{D\bar{D}} > 0$ Riemann sheet. That this state, corresponding to the $\chi_{c2}(1P)$, appears as a resonance with a tiny width is due to the forcing of a nonzero $\eta_c\eta$ coupling as described above—this state can appear as a bound-state pole in amplitude variations that do not have this constraint.

In Fig. 3 we present S-wave amplitudes for a range of K-matrix parametrizations found to be capable of describing the finite-volume spectrum (presented in Appendix B), where we observe that the finite-volume spectra have constrained quite tightly the weak magnitude of scattering, and the high degree of channel decoupling.

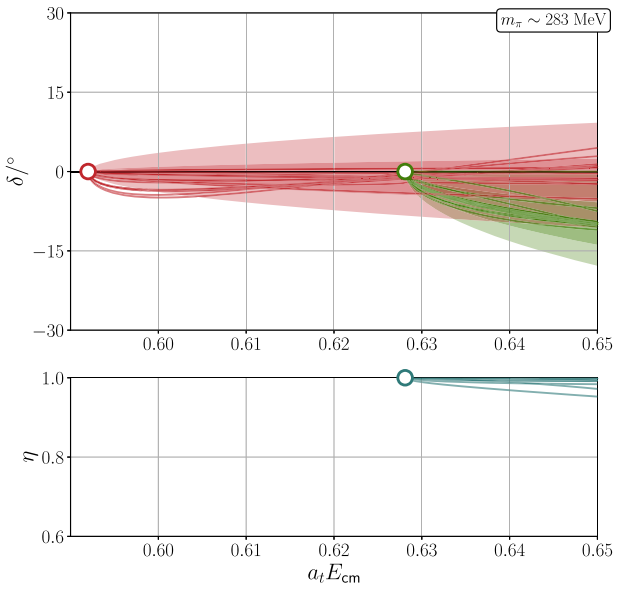


FIG. 3. S-wave coupled-channel phase shifts, $\delta_{\eta_c\eta}$, $\delta_{D\bar{D}}$, and inelasticity η, as defined in the caption of Fig. 2, for a range of amplitude parametrizations capable of describing the finite-volume spectrum (Tables VI and VII). For the amplitude given in Eq. (3), the uncertainty bands are shown (inner band is the statistical uncertainty, outer band includes also the impact of varying the masses and anisotropy as described in the text). For other amplitude parametrizations, only the central value curves are plotted.

B. $m_\pi \sim 239$ MeV and $m_\pi \sim 330$ MeV

The lighter and heavier pion mass lattices have only a single volume each, and a smaller number of discrete finite-volume energies with which to constrain scattering amplitudes, as can be seen in Fig. 1. As in the $m_\pi \sim 283$ MeV case we limit our attention to energies lying below a cutoff slightly below the $\psi\omega$ threshold.

In the $m_\pi \sim 239$ MeV case there are only five energy levels with dominant overlap onto $D\bar{D}$-like operators in the irreps dominated by S-wave scattering, which limits the degree to which we can consider amplitude parametrization variations. As was the case for $m_\pi \sim 283$ MeV there are no obvious indications in the spectrum for strong interactions in either $\eta_c\eta$ or $D\bar{D}$, and a description in terms of a constant K-matrix with assumed $\eta_c\eta - D\bar{D}$ decoupling gives

$$\begin{aligned} \gamma^{(S)}_{\eta_c\eta,\eta_c\eta} &= (0.69 \pm 0.18 \pm 0.74) \\ \gamma^{(S)}_{D\bar{D},D\bar{D}} &= (0.07 \pm 0.19 \pm 0.00) \\ \gamma^{(D)}_{\eta_c\eta,\eta_c\eta}/a_t^4 &= (-0.66 \pm 0.13 \pm 0.58) \times 10^3 \\ \gamma^{(D)}_{D\bar{D},D\bar{D}}/a_t^4 &= (4.0 \pm 0.3 \pm 1.7) \times 10^3 \end{aligned} \quad \begin{bmatrix} 1 & 0.42 & -1.00 & 0.02 \\ & 1 & -0.42 & 0.01 \\ & & 1 & -0.02 \\ & & & 1 \end{bmatrix} \tag{6}$$

$$\chi^2/N_{\text{dof}} = \tfrac{11.4}{18-4-6} = 1.42,$$

and as shown in Fig. 4 (left) this corresponds to S-wave scattering that is compatible with zero for both $\eta_c\eta$ and $D\bar{D}$.

In the $m_\pi \sim 330$ MeV case, the use of a smaller volume leads to a relatively modest total number of energy levels, and only three energy levels with dominant overlap onto $D\bar{D}$-like operators in the irreps dominated by S-wave scattering. A description of the spectrum using a constant decoupled K-matrix, as above, yields

$$\begin{aligned} \gamma^{(S)}_{\eta_c\eta,\eta_c\eta} &= (0.58 \pm 0.16 \pm 0.30) \\ \gamma^{(S)}_{D\bar{D},D\bar{D}} &= (-0.07 \pm 0.28 \pm 0.20) \\ \gamma^{(D)}_{\eta_c\eta,\eta_c\eta}/a_t^4 &= (0.34 \pm 0.13 \pm 0.60) \times 10^3 \\ \gamma^{(D)}_{D\bar{D},D\bar{D}}/a_t^4 &= (0.27 \pm 0.22 \pm 0.11) \times 10^3 \end{aligned} \quad \begin{bmatrix} 1 & 0.32 & 0.44 & 0.20 \\ & 1 & 0.21 & 0.52 \\ & & 1 & 0.13 \\ & & & 1 \end{bmatrix} \tag{7}$$

$$\chi^2/N_{\text{dof}} = \tfrac{18.9}{15-4} = 1.72,$$

and as shown in Fig. 4 this again indicates scattering that is very weak in both $\eta_c\eta$ and $D\bar{D}$.

In summary, while we are not as heavily overconstrained in determination of scattering in the $m_\pi \sim 239$ MeV and 330 MeV cases as we were in the 283 MeV case, we still observe the same behavior, that of scattering which is compatible with being decoupled between $\eta_c\eta$ and $D\bar{D}$, and very weak in both. There are no indications for bound states or resonances lying close to the $D\bar{D}$ threshold.

V. DECOUPLED $D\bar{D}$ S-WAVE SCATTERING AS A FUNCTION OF m_π

The amplitude descriptions of the previous section indicate no evidence for channel coupling between $D\bar{D}$ and $\eta_c\eta$ at any considered light quark mass, motivating a presentation of $D\bar{D}$ scattering near its kinematic threshold as an effectively *elastic* process. It is common to plot S-wave elastic scattering straddling the threshold by

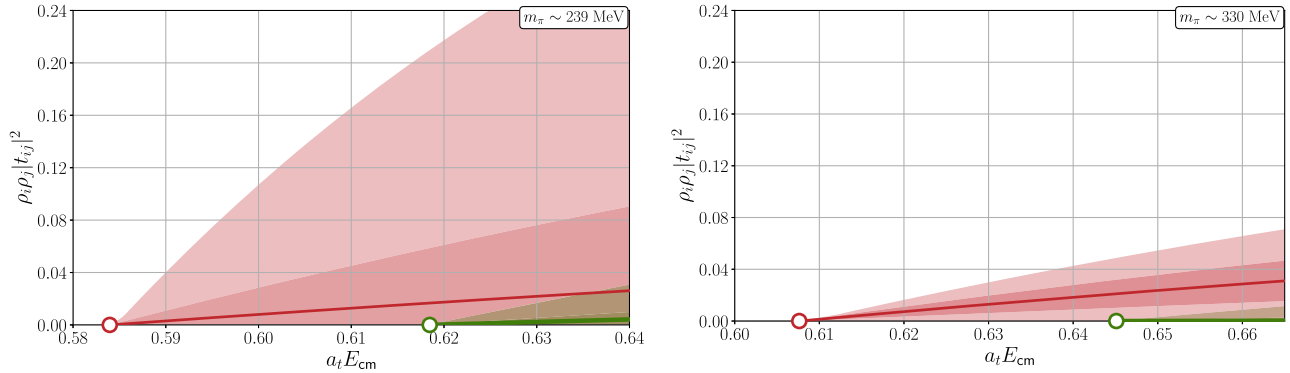


FIG. 4. S-wave scattering amplitudes for $m_\pi \sim 239$ MeV (left) and 330 MeV (right). Same color coding as in top panels of Fig. 2.

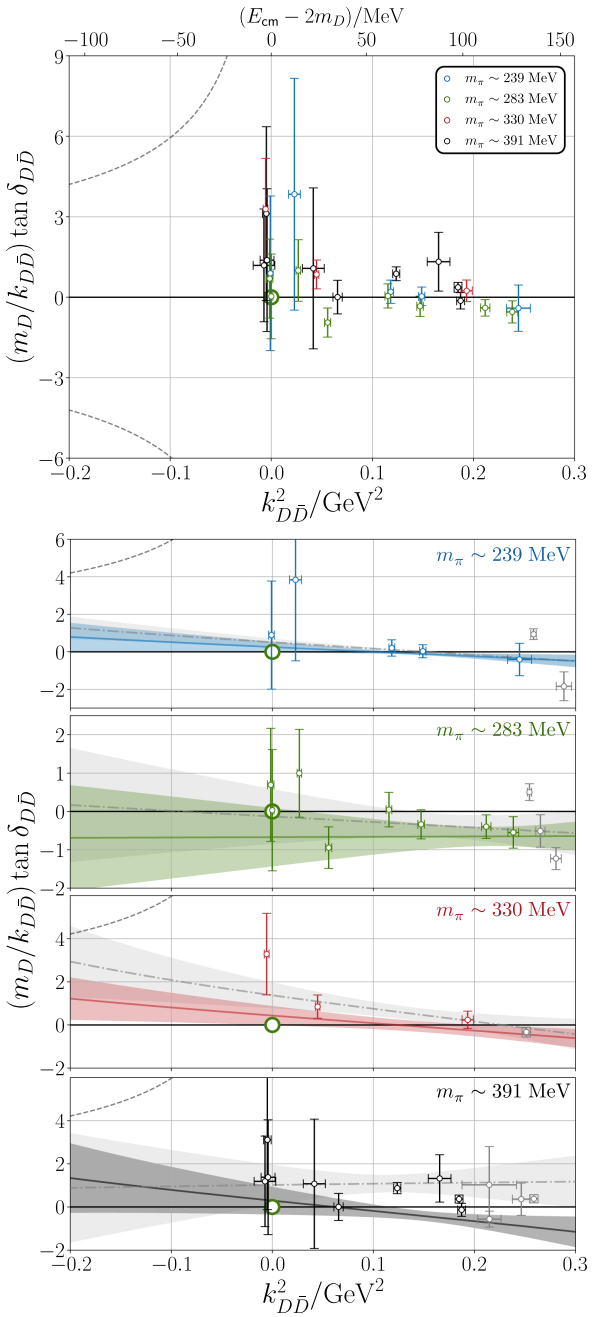


FIG. 5. $D\bar{D}$ amplitudes plotted as $(m_D/k)\tan\delta$, with decoupled S-wave $D\bar{D}$ interactions. The large green circle shows the location of $D\bar{D}$ threshold. The energy level points selected have overlaps dominated by $D\bar{D}$ operators, and the D-wave has been fixed to zero in the quantization condition. The gray points are above the energy cutoff used in the fits for each lattice. The dashed gray curves on the left show $\pm m_D/|k|$ below threshold. We have removed four points from this plot for the $m_\pi \sim 391$ MeV case which have very large uncertainties. The gray bands and dot-dashed curves show amplitudes determined neglecting energy level correlations.

means of the quantity $k\cot\delta_0$, which has the effective-range expansion, $a_0^{-1} + \frac{1}{2}r_0k^2 + \cdots$, and which intersects $\pm\sqrt{-k^2}$ below threshold in the case of a bound state (minus-sign choice) or a virtual-bound state (plus-sign choice). For the current case we have very weak scattering at threshold, characterized by small values of the scattering length, a_0, and as such a clearer presentation is given by plotting $k^{-1}\tan\delta_0$, which we may render dimensionless by scaling with the D-meson mass.

Figure 5 shows the subset of energy levels in the $[000]A_1^+$ and $[001]A_1$ irreps which have dominant overlap with $D\bar{D}$-like operators. The relevant value of δ_0 for each energy is computed assuming complete decoupling of the $\eta_c\eta$ channel, and zero amplitude for D-wave $D\bar{D}$ scattering at those energies. The upper panel indicates that there is no significant systematic dependence upon m_π across the range from 239 MeV to 391 MeV. As well as the discrete points, the lower panels also show curves illustrating one particular parametrization considered in the previous section, fitted to the entire spectrum across all computed irreps, including $\eta_c\eta$-dominated levels.[8] These curves generally match the behavior of the discrete points, with the apparent discrepancy at intermediate energies in the $m_\pi \sim 391$ MeV case, and the systematically low fit in the $m_\pi \sim 330$ MeV case, being due to strong data correlations—fits which neglect data correlation are also shown for comparison. We summarize these amplitudes in Appendix C.

When plotted as $k^{-1}\tan\delta_0$ versus k^2, the presence of a bound state would correspond to an intersection of the amplitude with the curve $-(-k^2)^{-1/2}$, while a virtual-bound state would present through an intersection with $+(-k^2)^{-1/2}$. These curves are shown in Fig. 5 as dashed lines below threshold, and it is quite clear that the lattice QCD energy levels and amplitude descriptions following from them do not support any nearby bound state or virtual-bound state at any of the pion masses computed.

The strength of $D\bar{D}$ scattering at threshold can be characterized by an S-wave scattering length, $a_0^{D\bar{D}}$ defined as $\lim_{\sqrt{s}\to 2m_D} t^{(\ell=0)}_{D\bar{D},D\bar{D}}(s)$. In the case that $D\bar{D}$ was coupled to the open $\eta_c\eta$ channel the scattering length would take a complex value, but will be real if the channels are decoupled. At all pion masses considered we find that for decoupled scattering amplitude descriptions we have $m_D \cdot |a_0^{D\bar{D}}| \lesssim 1$, with a slight preference for a small *negative* value in the best-constrained case of $m_\pi \sim 283$ MeV. For comparison, the 4 MeV $D\bar{D}$ bound state claimed in Ref. [27] would correspond to a scattering length $m_D \cdot a_0^{D\bar{D}} \approx -22$.

[8]But excluding the $c\bar{c}(1P)$-identified levels. The particular amplitude choice is decoupled between $D\bar{D}$ and $\eta_c\eta$ with the $D\bar{D}$ S-wave described by a K-matrix element with both $\gamma^{(0)}$ and $\gamma^{(1)}$ terms, while the $D\bar{D}$ D-wave and the $\eta_c\eta$ S-wave and D-wave K-matrix elements are described by constants. The $m_\pi \sim 283$ MeV case (with spectrum correlations) is given in Eq. (4).

VI. INTERPRETATION

The interpretation of the results of the calculation presented in this paper is quite simple: there is no evidence for strong scattering of $D\bar{D}$ in S-wave near threshold for pion masses between 239 MeV and 391 MeV. No pole singularities corresponding to bound states or resonances are needed to describe the weak scattering observed. References [24,25] determined coupled-channel amplitudes at $m_\pi \sim 391$ MeV to higher energies, above the $D_s\bar{D}_s$ threshold, and found that a single narrow resonance was required, in line with the expectations of the $c\bar{c}$ quark model for a $2P$ state.

A previous lattice QCD computation, Ref. [27], which used lattices on which $m_\pi \sim 280$ MeV, drew drastically different conclusions from those given above. This prior work chose to neglect the existence of the open $\eta_c\eta$ channel, computing correlation functions with $D\bar{D}$-like, $D_s\bar{D}_s$-like, and $c\bar{c}$-like operators.[9] In light of our demonstration in this paper of complete decoupling with the $\eta_c\eta$ channel, this assumption is unlikely to have been a significant source of error. Reference [27] concluded that their computed spectrum demanded the presence of a bound state 4 MeV below the $D\bar{D}$ threshold, with this being largely driven by their lowest $D\bar{D}$-like levels appearing significantly below the lowest noninteracting energies in two irreps (e.g., $D\bar{D}$ threshold in the rest frame). Such an observation is not seen at any of the pion masses computed in this paper, where the lowest $D\bar{D}$-like levels lie extremely close to the noninteracting energies, and we find no place for such a bound state.

As well as the bound state below $D\bar{D}$ threshold, and a "broad" resonance decaying to $D\bar{D}$, Ref. [27] also proposed a nearly stable state sitting right at $D_s\bar{D}_s$ threshold, apparently almost completely decoupled from $D\bar{D}$. We have not explored amplitudes in this energy region directly in this paper, but it would be surprising if the $D_s\bar{D}_s$ system, containing no valence light quarks, depended strongly on the light quark mass, and no such near-stable state was found in the calculation at $m_\pi \sim 391$ MeV in Refs. [24,25]. In the spectrum of higher-lying discrete energy levels computed in the current calculation for $m_\pi \sim 283$ MeV, but not used in amplitude determination, we do not see any obvious need for such a state.

A set of technical differences between the current calculation and that reported on in Ref. [27] which could contribute to the difference in determined spectra is discussed in Appendixes D and E. A plausible candidate is the difference in lattice spacing which may lead to discretization effects of differing magnitude. Within the calculation presented in this paper, done at (essentially) a single value of the lattice spacing, we see no evidence of discretization effects that impact our analysis, while in Ref. [50], which used the same lattices as Ref. [27], significant discretization effects were highlighted.

The current PDG [26] interpretation of the scalar resonance sector below 4 GeV, based upon the full set of contemporary experimental results, has a single "established" narrow resonance, $\chi_{c0}(3915)$, lying just below $D_s\bar{D}_s$ threshold, decaying to $D\bar{D}$ and $J/\psi\omega$ and contributing to a threshold peak in $D_s\bar{D}_s$ (observed in $B^+ \to K^+ D_s\bar{D}_s$ in Ref. [4]). Such a state could plausibly evolve into the single narrow resonance predicted at $m_\pi \sim 391$ MeV in Refs. [24,25] as the light quark mass is increased.[10]

The only other scalar resonance candidate listed in the PDG, which is not considered to be "established," is the rather broad $\chi_{c0}(3860)$ claimed to decay into $D\bar{D}$ in $e^+e^- \to J/\psi D\bar{D}$ [5]. At the pion masses explored in this paper there is no sign of any amplitude behavior consistent with the presence of such a state.

VII. SUMMARY

We have explored the scattering of $D\bar{D}$ meson pairs in the region around the kinematic threshold, allowing for possible coupling to the open $\eta_c\eta$ channel, but finding that there is no evidence that the two channels couple at any significant level. Exploring a range of light quark masses corresponding to pion masses between 239 and 330 MeV (supplemented by results previously obtained at 391 MeV in Refs. [24,25]), we find no significant interaction strength is present. In particular the results suggest no evidence of a near-threshold bound, virtual or resonant χ_{c0} state.

Descriptions of the $D\bar{D}$ system at threshold which demand a bound state [7,16,17,53], or a broader resonance (similar to the experimental candidate $\chi_{c0}(3860)$) [54] are not supported by the results of this calculation.

An important caveat is that this work has been performed with only a single value of the gauge coupling, and therefore lattice spacings across the different light quark masses are all close to a single value. While no obviously relevant indications of discretization effects have been observed, a systematic estimation of their scale is warranted in the future. In addition, the operator basis used included none that resemble compact tetraquark constructions; however an earlier study using the same action and the same kind of optimized meson-meson operators suggested that these may not be required to obtain a reliable spectrum in this approach [41].

This work indicates that isospin-0 S-wave scattering of $D\bar{D}$ close to threshold is *much* simpler than the

[9]The lowest lying $D^*\bar{D}^*$-like and $J/\psi\omega$-like operators were also included.

[10]The resonance in Refs. [24,25] lies above the $D_s\bar{D}_s$ threshold, but taking the amplitudes in Refs. [24,25] and simply lowering slightly the K-matrix mass parameter such that the resonance lies just below the $D_s\bar{D}_s$ threshold would lead to a rapid turn on of $D_s\bar{D}_s$ amplitudes at threshold due to the large resonance coupling to that channel. Similar suggestions can be found in Refs. [51,52].

corresponding light-quark channels, $\pi\pi$ or $K\bar{K}$, with consistent behavior seen for a range of light-quark masses. Considered alongside the results presented in Refs. [24,25] we have a demonstration, grounded in first-principles QCD, that the next scalar resonance above the $\chi_{c0}(1P)$ is likely to lie above 3900 MeV, with nothing of significance appearing in scattering amplitudes in between.

ACKNOWLEDGMENTS

We thank our colleagues within the Hadron Spectrum Collaboration (www.hadspec.org), in particular Daniel Yeo for careful reading of the manuscript. D. J. W. acknowledges support from a Royal Society University Research Fellowship. D. J. W. and C. E. T. acknowledge support from the U.K. Science and Technology Facilities Council (STFC) [Grant No. ST/X000664/1]. J. J. D. acknowledges support from the U.S. Department of Energy Contract No. DE-SC0018416 at William & Mary, and R. G. E. from Contract No. DE-AC05-06OR23177, under which Jefferson Science Associates, LLC, manages and operates Jefferson Lab. This work contributes to the goals of the U.S. Department of Energy ExoHad Topical Collaboration, Contract No. DE-SC0023598. Some software codes used in this project were developed with support from the U.S. Department of Energy, Office of Science, Office of Advanced Scientific Computing Research and Office of Nuclear Physics, Scientific Discovery through Advanced Computing (SciDAC) program; also acknowledged is support from the Exascale Computing Project (No. 17-SC-20-SC), a collaborative effort of the U.S. Department of Energy Office of Science and the National Nuclear Security Administration. This work used the Cambridge Service for Data Driven Discovery (CSD3), part of which is operated by the University of Cambridge Research Computing Service (www.csd3.cam.ac.uk) on behalf of the STFC DiRAC HPC Facility (www.dirac.ac.uk). The DiRAC component of CSD3 was funded by BEIS capital funding via STFC capital Grants No. ST/P002307/1 and No. ST/R002452/1 and STFC operations Grant No. ST/R00689X/1. Other components were provided by Dell EMC and Intel using Tier-2 funding from the Engineering and Physical Sciences Research Council (capital Grant No. EP/P020259/1). This work also used the earlier DiRAC Data Analytic system at the University of Cambridge. This equipment was funded by BIS National E-infrastructure capital Grant (No. ST/K001590/1), STFC capital Grants No. ST/H008861/1 and No. ST/H00887X/1, and STFC DiRAC Operations Grant No. ST/K00333X/1. DiRAC is part of the National E-Infrastructure. This work also used clusters at Jefferson Laboratory under the USQCD Initiative and the LQCD ARRA project. Propagators and gauge configurations used in this project were generated using DiRAC facilities, at Jefferson Lab, and on the Wilkes GPU cluster at the University of Cambridge High Performance Computing Service, provided by Dell Inc., NVIDIA and Mellanox, and part funded by STFC with industrial sponsorship from Rolls Royce and Mitsubishi Heavy Industries. Also used was an award of computer time provided by the U.S. Department of Energy INCITE program and supported in part under an ALCC award, and resources at the Oak Ridge Leadership Computing Facility, which is a DOE Office of Science User Facility supported under Contract No. DE-AC05-00OR22725; the National Energy Research Scientific Computing Center (NERSC), a U.S. Department of Energy Office of Science User Facility located at Lawrence Berkeley National Laboratory, operated under Contract No. DE-AC02-05CH11231; the Texas Advanced Computing Center (TACC) at The University of Texas at Austin; the Extreme Science and Engineering Discovery Environment (XSEDE), which is supported by National Science Foundation Grant No. ACI-1548562; and part of the Blue Waters sustained-petascale computing project, which is supported by the National Science Foundation (Awards No. OCI-0725070 and No. ACI-1238993) and the state of Illinois. Blue Waters is a joint effort of the University of Illinois at Urbana-Champaign and its National Center for Supercomputing Applications. The software codes Chroma [55], QUDA [56,57], QUDA-MG [58], QPhiX [59], MG-PROTO [60], QOPQDP [61,62], and Redstar [63] were used.

DATA AVAILABILITY

The data that support the findings of this article are not publicly available. The data are available from the authors upon reasonable request.

APPENDIX A: OPERATOR BASIS

In this section we present the basis of interpolating operators that were used to produce the matrices of correlation functions that form the input of our variational analyses. For $m_\pi \sim 283$ MeV see Table IV and for $m_\pi \sim 239$ MeV and $m_\pi \sim 330$ MeV see Table V. Details of the operator basis can be found in Refs. [24,25] and references therein.

APPENDIX B: AMPLITUDE PARAMETRIZATION VARIATIONS FOR $m_\pi \sim 283$ MeV

Tables VI and VII show the various parametrizations used to describe the finite-volume spectra excluding (Table VI) and including (Table VII) the $c\bar{c}(1P)$ deeply bound energy levels. The resulting amplitudes are plotted in Fig. 3.

TABLE IV. Operators used in the $m_\pi \sim 283$ MeV variational analyses.

$[000]A_1^+$	
$L/a_s = 24$	$L/a_s = 32$
$\bar{q}\Gamma q \times 7$	$\bar{q}\Gamma q \times 7$
$\eta_c[000]\eta[000]$	$\eta_c[000]\eta[000]$
$\eta_c[001]\eta[001]$	$\eta_c[001]\eta[001]$
$\eta_c[011]\eta[011]$	$\eta_c[011]\eta[011]$
	$\eta_c[111]\eta[111]$
	$\eta_c[002]\eta[002]$
$D[000]\bar{D}[000]$	$D[000]\bar{D}[000]$
$D[001]\bar{D}[001]$	$D[001]\bar{D}[001]$
	$D[011]\bar{D}[011]$
	$D[111]\bar{D}[111]$
$D_s[000]\bar{D}_s[000]$	$D_s[000]\bar{D}_s[000]$
$\psi[000]\omega[000]$	$\psi[000]\omega[000]$
$[001]A_1$	
$L/a_s = 24$	$L/a_s = 32$
$\bar{q}\Gamma q \times 10$	$\bar{q}\Gamma q \times 11$
$\eta_c[001]\eta[000]$	$\eta_c[001]\eta[000]$
$\eta_c[000]\eta[001]$	$\eta_c[000]\eta[001]$
$\eta_c[011]\eta[001]$	$\eta_c[011]\eta[001]$
$\eta_c[002]\eta[001]$	$\eta_c[002]\eta[001]$
$\eta_c[001]\eta[011]$	$\eta_c[001]\eta[011]$
$\eta_c[111]\eta[011]$	$\eta_c[111]\eta[011]$
	$\eta_c[012]\eta[011]$
	$\eta_c[011]\eta[111]$
	$\eta_c[001]\eta[002]$
	$\eta_c[112]\eta[111]$
$D[000]\bar{D}[001]$	$D[000]\bar{D}[001]$
$D[001]\bar{D}[011]$	$D[001]\bar{D}[011]$
	$D[001]\bar{D}[002]$
	$D[011]\bar{D}[111]$
$[000]E^+$	
$L/a_s = 24$	$L/a_s = 32$
$\bar{q}\Gamma q \times 10$	$\bar{q}\Gamma q \times 8$
$\eta_c[001]\eta[001]$	$\eta_c[001]\eta[001]$
$\eta_c[011]\eta[011]$	$\eta_c[011]\eta[011]$
	$\eta_c[002]\eta[002]$
$D[001]\bar{D}[001]$	$D[001]\bar{D}[001]$
$D[011]\bar{D}[011]$	$D[011]\bar{D}[011]$
$\psi[000]\omega[000]$	$\psi[000]\omega[000]$

TABLE V. Operators used in the variational analyses. Top: $m_\pi \sim 239$ MeV, $L/a_s = 32$. Bottom: $m_\pi \sim 330$ MeV, $L/a_s = 24$.

$[000]A_1^+$	$[001]A_1$	$[000]E^+$
$\bar{q}\Gamma q \times 7$	$\bar{q}\Gamma q \times 14$	$\bar{q}\Gamma q \times 11$
$\eta_c[000]\eta[000]$	$\eta_c[001]\eta[000]$	$\eta_c[001]\eta[001]$
$\eta_c[001]\eta[001]$	$\eta_c[000]\eta[001]$	$\eta_c[011]\eta[011]$
$\eta_c[011]\eta[011]$	$\eta_c[011]\eta[001]$	$\eta_c[002]\eta[002]$
$\eta_c[111]\eta[111]$	$\eta_c[002]\eta[001]$	
$\eta_c[002]\eta[002]$	$\eta_c[001]\eta[011]$	
	$\eta_c[111]\eta[011]$	
	$\eta_c[012]\eta[011]$	
	$\eta_c[011]\eta[111]$	
	$\eta_c[001]\eta[002]$	
	$\eta_c[112]\eta[111]$	
$D[000]\bar{D}[000]$	$D[000]\bar{D}[001]$	$D[001]\bar{D}[001]$
$D[001]\bar{D}[001]$	$D[001]\bar{D}[011]$	$D[011]\bar{D}[011]$
$D[011]\bar{D}[011]$	$D[001]\bar{D}[002]$	$D[002]\bar{D}[002]$
$D[111]\bar{D}[111]$	$D[011]\bar{D}[111]$	
$D_s[000]\bar{D}_s[000]$		$D_s[001]\bar{D}_s[001]$
		$D[011]\bar{D}^*[011]$
$\psi[000]\omega[000]$		$\psi[000]\omega[000]$

$[000]A_1^+$	$[001]A_1$	$[000]E^+$
$\bar{q}\Gamma q \times 9$	$\bar{q}\Gamma q \times 11$	$\bar{q}\Gamma q \times 10$
$\eta_c[000]\eta[000]$	$\eta_c[001]\eta[000]$	$\eta_c[001]\eta[001]$
$\eta_c[001]\eta[001]$	$\eta_c[000]\eta[001]$	$\eta_c[011]\eta[011]$
$\eta_c[011]\eta[011]$	$\eta_c[011]\eta[001]$	
	$\eta_c[002]\eta[001]$	
	$\eta_c[001]\eta[011]$	
	$\eta_c[111]\eta[011]$	
	$\eta_c[012]\eta[011]$	
	$\eta_c[011]\eta[111]$	
$D[000]\bar{D}[000]$	$D[000]\bar{D}[001]$	$D[001]\bar{D}[001]$
$D[001]\bar{D}[001]$	$D[001]\bar{D}[011]$	$D[011]\bar{D}[011]$
	$D[011]\bar{D}[111]$	
$D_s[000]\bar{D}_s[000]$	$D_s[000]\bar{D}_s[001]$	$D_s[001]\bar{D}_s[001]$
		$D[011]\bar{D}^*[011]$
		$D^*[000]\bar{D}^*[000]$
$\psi[000]\omega[000]$		$\psi[000]\omega[000]$

APPENDIX C: $D\bar{D}$ AMPLITUDES FROM DECOUPLED LINEAR K-MATRIX PARAMETRIZATIONS, APPEARING IN FIG. 5

In Table VIII, we summarize the S-wave amplitudes presented in Fig. 5. For each light quark mass, we consider both a correlated χ^2 fit and, for visual comparison, one where the energy correlations are discarded. The amplitude form is the same as that used in Eq. (4), as defined in Eq. (2), with a Chew-Mandelstam phase space that is subtracted at $D\bar{D}$ threshold. With this fit form the fit parameter $\gamma^{(0)}_{D\bar{D}}$ is equal to $m_D a^{D\bar{D}}_{\ell=0}$, where $a^{D\bar{D}}_{\ell=0}$ is the S-wave $D\bar{D}$ scattering length.

We include fits with an uncorrelated χ^2 to illustrate that the apparent systematic difference between the points and curves in Fig. 5 is due to data correlation—when these correlations are ignored the fit curves are in good visual agreement with the points. Both correlated and uncorrelated fits indicate very weak interactions at threshold.

TABLE VI. Parametrization variations. Channel labels: $1 \to \eta_c\eta$, $2 \to D\bar{D}$, CM: Chew-Mandelstam, $-i\rho$: simple phase space.

S-wave parameters						D-wave parameters			Phase space		
$\gamma_{1,1}^{(S)(0)}$	$\gamma_{1,1}^{(S)(1)}$	$\gamma_{1,2}^{(S)(0)}$	$\gamma_{1,2}^{(S)(1)}$	$\gamma_{2,2}^{(S)(0)}$	$\gamma_{2,2}^{(S)(1)}$	$\gamma_{1,1}^{(D)(0)}$	$\gamma_{1,2}^{(D)(0)}$	$\gamma_{2,2}^{(D)(0)}$	S	D	$\frac{\chi^2}{N_{\text{dof}}}$
Reference parametrization Eq. (3)											
✓		✓		✓		✓	✓	✓	CM	CM	$\frac{35.4}{34-6-3} = 1.41$
Parametrization variations using Eq. (2) with no poles											
✓		✓		✓		✓		✓	CM	CM	$\frac{35.4}{34-5-3} = 1.36$
✓		✓				✓	✓		CM	CM	$\frac{35.4}{34-4-3} = 1.31$
✓				✓		✓		✓	CM	CM	$\frac{35.4}{34-4-3} = 1.31$
✓			✓	✓		✓		✓	CM	CM	$\frac{35.4}{34-5-3} = 1.36$
✓				✓	✓	✓		✓	CM	CM	$\frac{35.4}{34-5-3} = 1.36$
✓					✓	✓		✓	CM	CM	$\frac{35.5}{34-4-3} = 1.31$
	✓			✓		✓		✓	CM	CM	$\frac{35.4}{34-4-3} = 1.31$
✓		✓		✓		✓	✓	✓	$-i\rho$	$-i\rho$	$\frac{35.4}{34-6-3} = 1.42$
✓				✓		✓		✓	$-i\rho$	$-i\rho$	$\frac{35.4}{34-4-3} = 1.31$

TABLE VII. Parametrization variations. Channel labels: $1 \to \eta_c\eta$, $2 \to D\bar{D}$, CM: Chew-Mandelstam, $-i\rho$: simple phase space.

S-wave parameters						D-wave parameters						Phase space		
m_S	$g_1^{(S)}$	$g_2^{(S)}$	$\gamma_{1,1}^{(S)}$	$\gamma_{1,2}^{(S)}$	$\gamma_{2,2}^{(S)}$	m_D	$g_1^{(D)}$	$g_2^{(D)}$	$\gamma_{1,1}^{(D)}$	$\gamma_{1,2}^{(D)}$	$\gamma_{2,2}^{(D)}$	S	D	$\frac{\chi^2}{N_{\text{dof}}}$
Parametrization from Eq. (5)														
✓	✓	✓	✓	✓		✓	✓		✓		✓	CM	CM	$\frac{32.1}{42-9-4} = 1.11$
Parametrization variations using Eq. (2) (including poles)														
✓	✓	✓	✓	✓	✓	✓	✓	✓	✓	✓	✓	CM	CM	$\frac{32.1}{42-12-4} = 1.23$
✓	✓	✓	✓	✓	✓	✓	✓	✓	✓		✓	CM	CM	$\frac{32.1}{42-11-4} = 1.19$
✓	✓		✓	✓	✓	✓	✓	✓	✓		✓	CM	CM	$\frac{32.1}{42-10-4} = 1.14$
✓	✓	✓	✓	✓	✓	✓	✓		✓		✓	CM	CM	$\frac{32.1}{42-10-4} = 1.14$
✓	✓	✓	✓	✓		✓	✓			✓	✓	CM	CM	$\frac{38.5}{42-9-4} = 1.33$
✓	✓	✓	✓			✓	✓			✓	✓	CM	CM	$\frac{39.6}{42-8-4} = 1.32$
✓	✓	✓				✓	✓			✓	✓	CM	CM	$\frac{39.7}{42-7-4} = 1.28$
✓	✓		✓	✓	✓	✓	✓			✓	✓	CM	CM	$\frac{39.9}{42-9-4} = 1.38$
✓	✓		✓		✓	✓	✓		✓		✓	CM	CM	$\frac{32.1}{42-8-4} = 1.07$
✓	✓		✓		✓	✓	✓		✓		✓	$-i\rho$	$-i\rho$	$\frac{32.1}{42-8-4} = 1.07$
✓	✓	✓	✓	✓	✓	✓	✓	✓	✓	✓	✓	$-i\rho$	$-i\rho$	$\frac{32.1}{42-12-4} = 1.23$
✓	✓	✓	✓	✓		✓	✓		✓		✓	$-i\rho$	$-i\rho$	$\frac{32.2}{42-9-4} = 1.11$
✓	✓	✓				✓	✓			✓	✓	$-i\rho$	$-i\rho$	$\frac{39.7}{42-7-4} = 1.28$

TABLE VIII. S-wave $D\bar{D}$ amplitudes determined using a linear decoupled two-channel K-matrix that are shown in Fig. 5. In the definitions used here $m_D a^{D\bar{D}}_{\ell=0} = \gamma^{(0)}_{D\bar{D}}$.

	239 MeV	283 MeV	330 MeV	391 MeV
correlated				
$\gamma^{(0)}_{D\bar{D}}$	0.18 ± 0.15	-0.67 ± 0.84	0.44 ± 0.47	0.29 ± 0.63
$\gamma^{(1)}_{D\bar{D}}$	-9.1 ± 1.1	0.2 ± 12.8	-12.5 ± 9.0	-17 ± 14
$\chi^2/N_{\rm dof}$	1.75	1.36	1.70	1.37
uncorrelated				
$\gamma^{(0)}_{D\bar{D}}$	0.51 ± 0.20	-0.13 ± 0.96	1.38 ± 0.60	1.02 ± 0.94
$\gamma^{(1)}_{D\bar{D}}$	-11.9 ± 6.0	-5 ± 17	-22 ± 14	3 ± 26
$\chi^2/N_{\rm dof}$	0.95	1.15	1.16	0.84

APPENDIX D: ADDITIONAL DETAILS AND COMPARISON OF RESULTS WITH PRELOVSEK *ET AL.*, REF. [27]

Reference [27] concludes a completely different spectrum of bound states and resonances, and strength of $D\bar{D}$ scattering from the current calculation, even when the quark mass is comparable at $m_\pi \sim 280$ MeV. These systematic differences with respect to Ref. [27] do not have an obvious explanation. The relatively large energy shifts with respect to finite-volume noninteracting energies found in Ref. [27] are what drive their amplitudes to contain the extra singularities, and as such we should attempt to identify what is causing the finite-volume spectrum to differ so significantly.

One possibility is that the extracted finite-volume energy levels in one or both studies are systematically biased, or have an underestimated systematic error. Their determination in principle depends upon the details of operator construction, the content of the operator basis, the procedure used to diagonalize the correlator matrix, and the time slice fitting of the correlator matrix eigenvalues. We will highlight some differences in approach between the calculation presented in this paper, and that in Ref. [27], although we lack sufficient information about the details of analysis used in Ref. [27] to make a full quantitative comparison.

In the current study, we make use of *optimized* single-hadron operators in the construction of hadron-hadron operators. They are optimized in the sense of having been determined by diagonalizing a matrix of correlation functions built using a basis of fermion bilinear operators, independently for each meson three-momentum [35]. Using these optimized operators in the pair products of hadron-hadron operators, we might expect more rapid relaxation to the finite-volume energies given the suppression of single-hadron excitations. In Refs. [64,65], differences in extracted finite-volume energy level values are seen when adding operators formed from a diquark-antidiquark construction to hadron-hadron constructions, when compared to using hadron-hadron constructions alone. Like Ref. [27], these studies use hadron-hadron operator constructions that use nonoptimized single-hadron operators in the product.

Figure 6 shows an example of the extraction of a finite-volume spectrum from the generalized eigenvalues of the matrix of correlation functions. The example shown is the $[000]A_1^+$ irrep on the 32^3 lattice at $m_\pi \sim 283$ MeV. For each eigenvalue at $t_0 = 10a_t$ we see behavior consistent with dominance of a single state at modest times. Each time dependence is fitted as a sum of two exponentials (and occasionally as a single exponential) for a range of time windows, and each fit has a quality associated with it as estimated by the Akaike information criterion (AIC). Our final determination for each $a_t E_{\mathfrak{n}}$ value comes from the "model average" over these determinations (see Ref. [66]). As can be seen from the blue points (AIC average) compared to the red points (single best time-window fit), this average typically provides a more conservative estimate. We note that the near-threshold $D\bar{D}$-operator dominated state (bottom left panel) has a principal correlator which very clearly relaxes to its long-time behavior rapidly and shows very little variation over time-window choice.

Figure 7 shows that the choice of t_0 value used in the solution of the generalized eigenvalue problem in this case has no significant impact upon the extracted energy spectrum.

Potentially important differences between the two calculations come from the details of the lattice setup, the lattice spacing, and the implementation of charm quarks. Reference [27] uses isotropic lattices with $a \approx 0.086$ fm, and while this is finer than our spatial spacing, it is much coarser than our temporal spacing. Using clover improved Wilson fermions to describe charm quarks, they report evidence for discretization effects in the form of departures from continuum relativistic dispersion relations for D-mesons. They choose to apply an *ad hoc* correction to deal with this in their finite-volume energy spectrum: for each determined energy level, after computing the energy gap from the nearest noninteracting $D\bar{D}$ energy (using D-meson energies as computed on the lattice) they then produce an absolute energy by reinstating the noninteracting energy after moving the D-meson energies to lie on the continuum dispersion relation. No additional systematic error is associated with this procedure, despite the adjustment in energy being typically larger than the statistical error on the energy level. This procedure impacts higher-lying energies, but does not significantly shift the levels at threshold in the rest frame, indicating that it alone cannot be the source of the differences with respect to the energy levels in the current paper.

In comparison, in the calculation reported on in this paper, we observe no systematic departures from the continuum relativistic dispersion form, *but* we have the additional

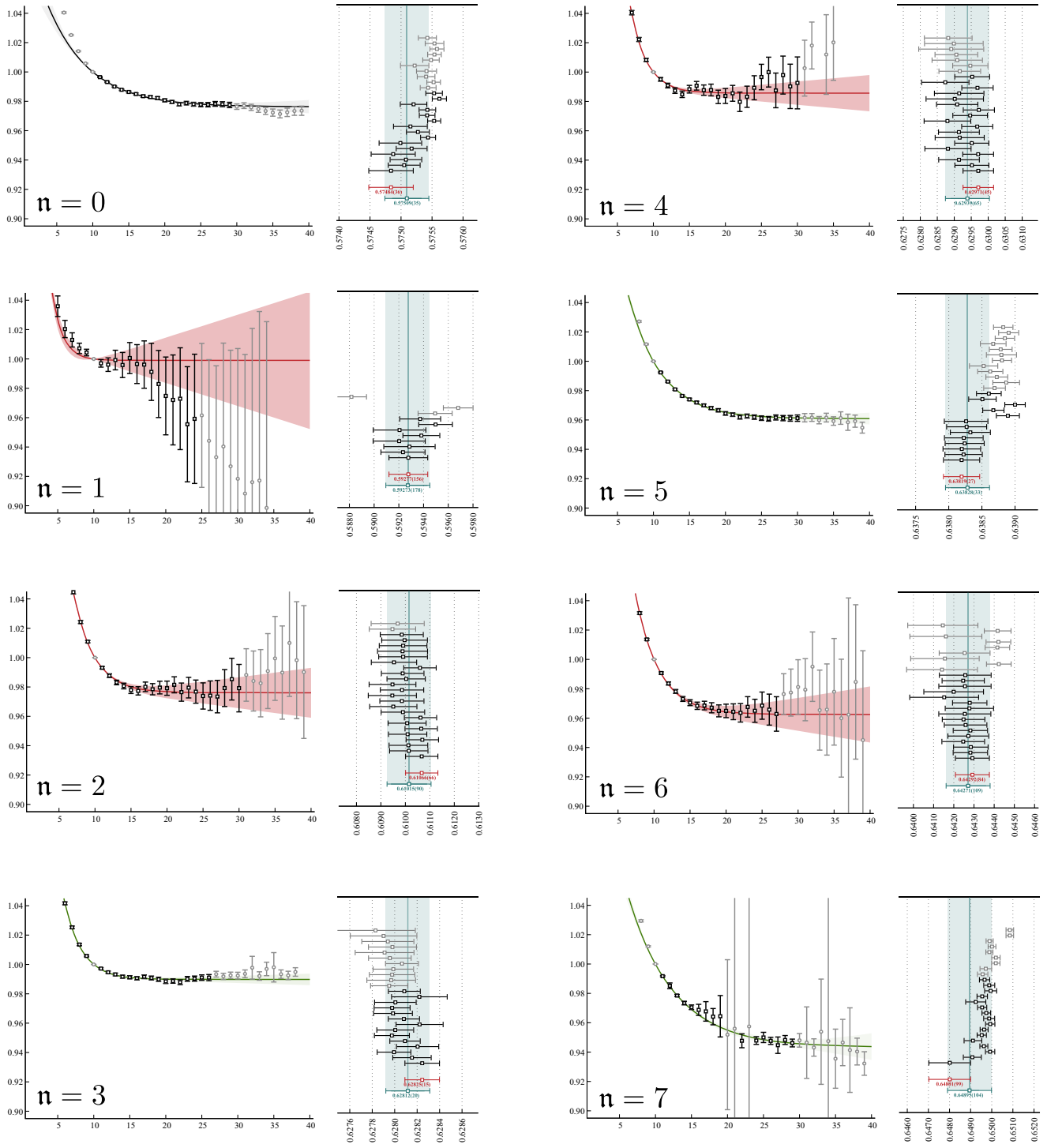


FIG. 6. Time slice fits to *principal correlators*, $\lambda_{\mathfrak{n}}(t)$, obtained from solving generalized eigenvalue problem, $\mathbf{C}(t)v_{\mathfrak{n}} = \lambda_{\mathfrak{n}}(t)\mathbf{C}(t_0)v_{\mathfrak{n}}$, with $t_0/a_t = 10$. Fit with $\lambda_{\mathfrak{n}}(t) = (1 - A_{\mathfrak{n}})e^{-E_{\mathfrak{n}}(t-t_0)} + A_{\mathfrak{n}}e^{-E'_{\mathfrak{n}}(t-t_0)}$. $m_\pi \sim 283$ MeV, 32^3 lattice, $[000]A_1^+$ irrep. Each panel shows, on left, $e^{E_{\mathfrak{n}}(t-t_0)}\lambda_{\mathfrak{n}}(t)$, with the best single time-window fit curve superimposed, and on the right the variation of extracted $a_t E_{\mathfrak{n}}$ over different fit windows, ordered from bottom up by decreasing value of AIC. Energy values with AIC probability $< 1\%$ are grayed out. The AIC model average value of $a_t E_{\mathfrak{n}}$ is shown by the blue point and band.

anisotropy parameter, ξ, to vary, and as presented in Sec. II this parameter varies slightly for different hadron species. We treat this variation conservatively by propagating the maximal deviations into our final amplitudes (see Table III).

Discretization effects are not expected to be limited to deviations from the relativistic dispersion relation, and from a calculation at a single lattice spacing we cannot determine with confidence their form or magnitude. We do

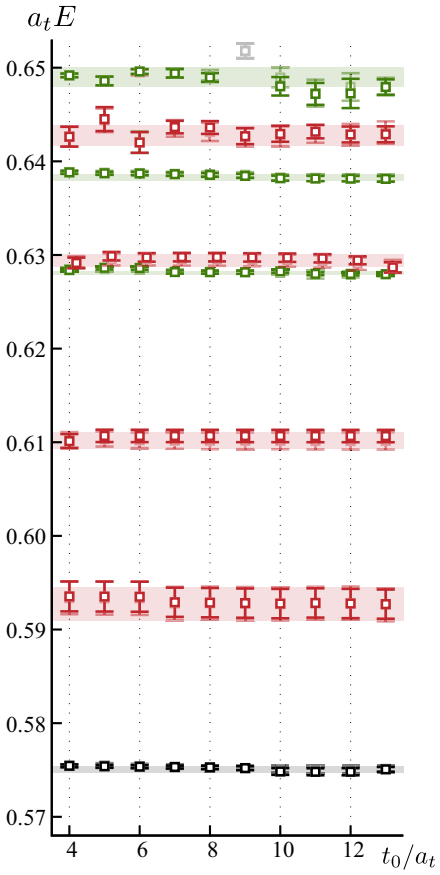


FIG. 7. In same case as Fig. 6, the variation of extracted E_n spectrum with changing choice of t_0. Solid points show the single best fit-window value, and the ghosted values show the AIC model average. Horizontal bands illustrate the $t_0 = 10a_t$ choice.

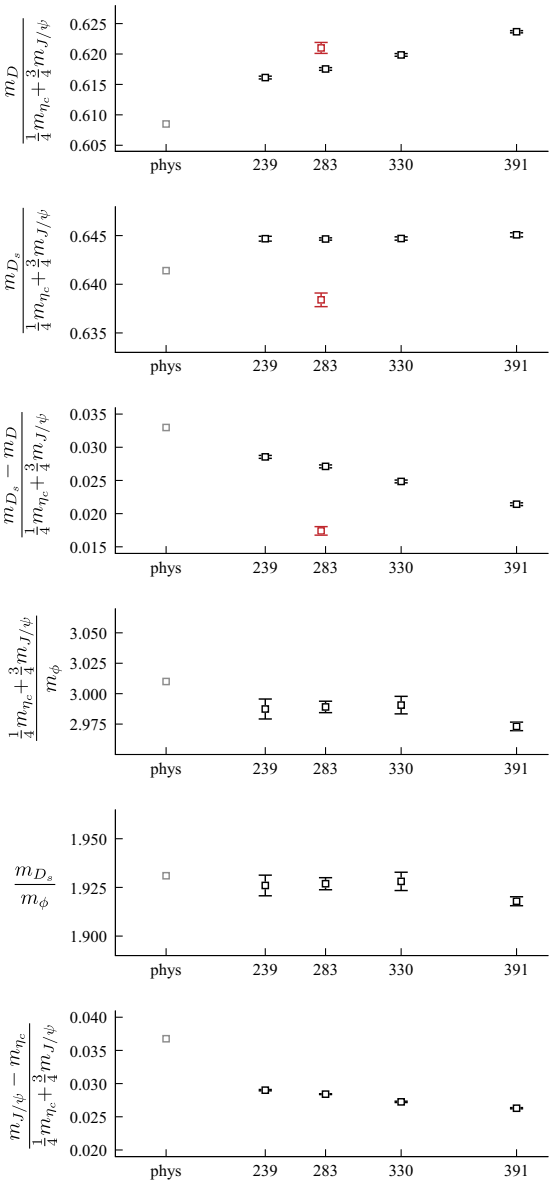


FIG. 8. Ratios of stable hadron masses as a function of m_π^2. Black points determined in the current paper and Refs. [24,25]. Gray points taken from PDG values. Red points from Ref. [27].

observe some systematic discrepancies which may originate in the lack of a continuum extrapolation, two of which are shown in Fig. 8. The bottom panel shows the "hyperfine splitting" scaled by the spin-averaged $1S$ charmonium mass as a function of light quark mass, which we observe to lie significantly below the experimental value, as has been observed previously [31,41,67,68]. The top panel shows the D-meson mass ratio with the spin-averaged $1S$ charmonium mass, which we note appears to extrapolate to about 0.3% above the physical value, indicating room for modest discretization effects at the few MeV level.

A reanalysis of the finite-volume spectrum of Ref. [27] was presented in Ref. [28] using amplitudes with improved analytic properties. While coming to quite similar conclusions about the pole content of the scattering system, this analysis had a great deal of difficulty describing both the rest-frame and moving-frame spectra simultaneously, having a $\chi^2/N_{\text{dof}} > 3$ and visibly large departures from the computed spectrum at energies near the $D\bar{D}$ threshold. Potentially this could indicate that the finite-volume spectra are not compatible with the description solely by scattering amplitudes in the finite-volume quantization condition—this would be the case if there were non-negligible discretization effects.

In Fig. 8 we show evidence that in the current calculation, the charm quark is tuned consistently at each of the three pion masses considered, particularly in the fourth and fifth panels. In these panels we also see an indication that the charm mass may have been tuned very slightly low on the 391 MeV lattice reported in Refs. [24,25]. The second panel illustrates the fact that the strange quark on the lattice used in Ref. [27] is tuned to be lighter than the physical strange quark mass, which has the impact of significantly reducing the region between the $D\bar{D}$ threshold and the $D_s\bar{D}_s$ threshold (see the third panel).

The smaller of the two volumes used in Ref. [27] has a spatial length in physical units of $L \sim 2.1$ fm and $m_\pi L \lesssim 3$, and while this might be considered to be on the small side, pions probably do not play a primary role in the scattering processes of interest, and there are no obvious systematic discrepancies between the smaller volume and the larger, $L \sim 2.8$ fm, lattice. In the current calculation, the smaller of the 283 MeV lattices is of a similar size in physical units to the larger lattice in Ref. [27].

Reference [27] observes a difference in the D-meson mass determined on the two volumes, at the level of 0.2%. As mentioned above, this variation is treated in an *ad hoc* way with no corresponding uncertainty added. In the current calculation, on the $m_\pi \sim 283$ MeV lattices we observe a D-meson difference of a similar magnitude, and we choose to associate an additional $a_t \delta E = 0.00050$ systematic error on every energy level to conservatively account for it.

APPENDIX E: CORRELATOR RATIOS

Reference [27] determines their inputs for Lüscher's method not by fitting correlation functions, but by forming a ratio of correlators and fitting that instead. From this, the energy difference between the noninteracting level and the level obtained from the correlation matrix (containing $D\bar{D}$ operators) can be determined. This assumes a perfect agreement with the continuum dispersion relation, even though there are differences that may reflect uncontrolled discretization effects. In this Appendix, we consider a ratio of principal correlators that mimics this approach somewhat, using the correlators obtained in this work.

For $[000]A_1^+$ on the $m_\pi \sim 283$ MeV ensembles, we consider the $\mathfrak{n} = 3$ correlator, which in both cases is dominated by a $D[000]\bar{D}[000]$ operator construction and lies very close to the noninteracting energy from the variational analysis. Dividing this by the ground-state $[000]A_1^-$ $D[000]$ principal correlator squared gives the ratio $R(t) = \lambda_{\mathfrak{n}=3}(t)/(\lambda_{D[000]}(t))^2$. It has been observed in a few studies that excited state effects largely cancel in this ratio. Generally those studies use only "simple" meson-meson operators where the D and $\bar{D}$-meson constituents are formed from a single operator ($\sim \bar{c}\gamma_5 \ell$). In this work, projected operators are used to form the meson-meson operators, and these are observed to reduce the excited-state contributions in the meson-meson correlators. Thus one does not expect a large effect at low t values.

To illustrate this, we plot "effective masses" for these quantities, both individually and as a ratio, in Fig. 9 using

$$a_t m_{\text{eff}} = \frac{1}{\delta t} \log \frac{C(t)}{C(t+\delta t)}, \tag{E1}$$

where we have chosen $\delta t / a_t = 3$. We work from the principal correlators $\lambda_{\mathfrak{n}}$ determined from the variational method in the main analysis. We summarize a few fits of

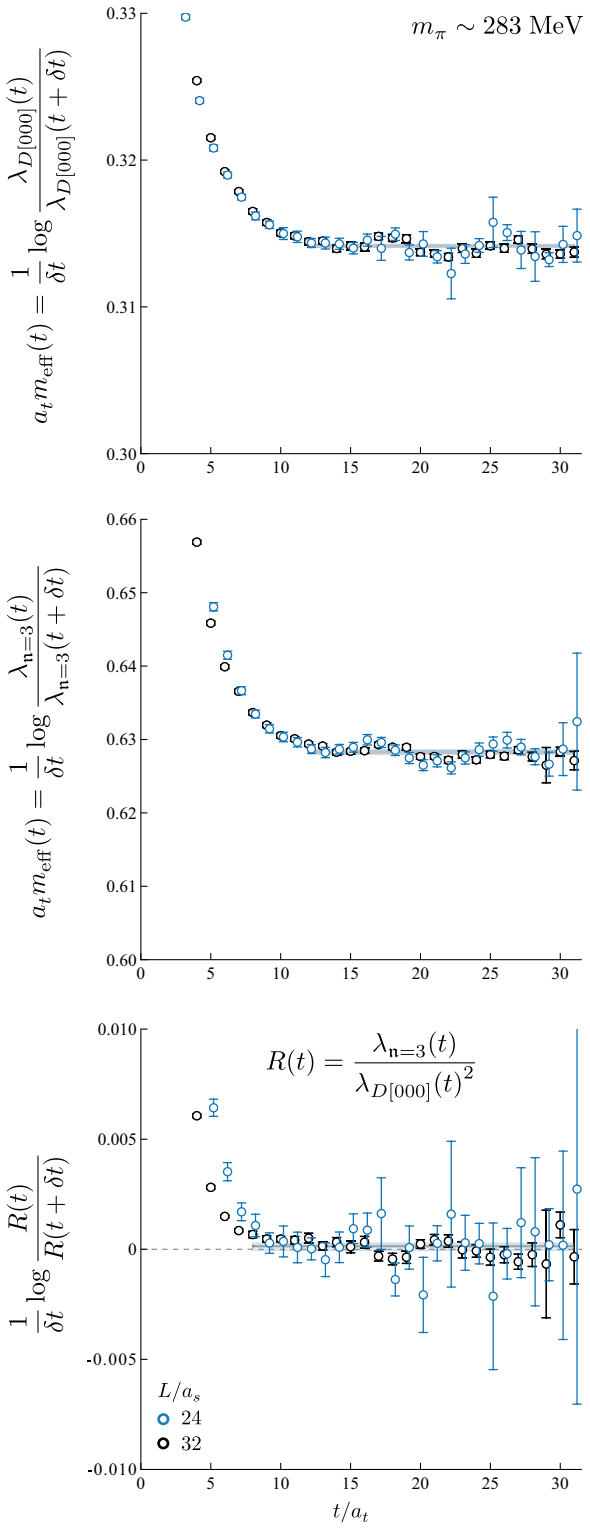


FIG. 9. "Effective masses" for the D-meson at rest (top), the $D[000]\bar{D}[000]$-dominated level (middle), and a ratio of these (bottom). Each quantity is derived from the principal correlators $\lambda_{\mathfrak{n}}(t)$ determined from the variational method analysis of correlation matrices. A representative fit is shown in each case, where the width shows the fit region and the vertical extent shows the value and uncertainty.

TABLE IX. A selection of principal correlator and effective mass fits around $D\bar{D}$ threshold on the $m_\pi \sim 283$ MeV lattices. $R(t) = \lambda_{\mathbf{n}=3}/\lambda^2_{D[000]}$ as described in the text.

	$m_{\text{eff}}(t)$	Fit range	χ^2/N
$L/a_s = 24$			
$\lambda_{D[000]}(t)$	0.31415(9)	[12, 31]	0.87
	0.31410(10)	[15, 31]	0.91
$\lambda_{\mathbf{n}=3}(t)$	0.62830(26)	[12, 31]	1.50
	0.62821(30)	[15, 31]	1.50
$R(t)$	0.00011(16)	[8, 31]	0.57
	−0.00005(19)	[12, 31]	0.39
	−0.00008(23)	[15, 31]	0.46
$L/a_s = 32$			
$\lambda_{D[000]}(t)$	0.31415(6)	[12, 31]	2.2
	0.31407(7)	[15, 31]	2.0
$\lambda_{\mathbf{n}=3}(t)$	0.62839(11)	[12, 31]	2.4
	0.62820(13)	[15, 31]	1.9
$R(t)$	0.00015(3)	[8, 31]	2.4
	0.00006(4)	[12, 31]	0.88
	0.00001(5)	[15, 31]	0.90

these using simple constants to the large time behavior in Table IX. A few different fit ranges are considered. In both cases, the numerators ($\lambda_{\mathbf{n}=3}$) match exactly those used in the main analysis above. We form the ratio under jackknife, averaged over the same time sources for numerator and denominator in order to allow any correlated fluctuations to cancel as much as possible. At large t values, we observe every quantity is dominated by a single exponential and thus tends to a constant in the effective mass equation (E1). For the ratio $R(t)$, this should correspond to the difference $\Delta E = E_{\mathbf{n}=3} - 2E_{D[000]}$.

We see that in this approach (where the systematic differences in D-meson masses are neglected) we do find smaller statistical uncertainties than reported in the main study. However, the differences $\Delta E = E_{\mathbf{n}=3} - 2E_{D[000]}$ are still very close to (or consistent with) zero, pointing to insignificant interactions at threshold.

[1] S. Uehara *et al.* (Belle Collaboration), Observation of a charmoniumlike enhancement in the $\gamma\gamma \to \omega J/\psi$ process, Phys. Rev. Lett. **104**, 092001 (2010).

[2] R. Aaij *et al.* (LHCb Collaboration), Near-threshold $D\bar{D}$ spectroscopy and observation of a new charmonium state, J. High Energy Phys. 07 (2019) 035.

[3] R. Aaij *et al.* (LHCb Collaboration), Amplitude analysis of the $B^+ \to D^+D^-K^+$ decay, Phys. Rev. D **102**, 112003 (2020).

[4] R. Aaij *et al.* (LHCb Collaboration), Observation of a resonant structure near the $D_s^+D_s^-$ threshold in the $B^+ \to D^+D^-K^+$ decay, Phys. Rev. Lett. **131**, 071901 (2023).

[5] K. Chilikin *et al.* (Belle Collaboration), Observation of an alternative $\chi_{c0}(2P)$ candidate in $e^+e^- \to J/\psi D\bar{D}$, Phys. Rev. D **95**, 112003 (2017).

[6] R. Molina and E. Oset, The Y(3940), Z(3930) and the X(4160) as dynamically generated resonances from the vector-vector interaction, Phys. Rev. D **80**, 114013 (2009).

[7] X.-K. Dong, F.-K. Guo, and B.-S. Zou, A survey of heavy-antiheavy hadronic molecules, Prog. Phys. **41**, 65 (2021).

[8] L. Maiani, F. Piccinini, A. D. Polosa, and V. Riquer, Diquark-antidiquarks with hidden or open charm and the nature of X(3872), Phys. Rev. D **71**, 014028 (2005).

[9] R. F. Lebed and A. D. Polosa, $\chi_{c0}(3915)$ As the lightest $c\bar{c}s\bar{s}$ state, Phys. Rev. D **93**, 094024 (2016).

[10] E. J. Eichten, K. Lane, and C. Quigg, New states above charm threshold, Phys. Rev. D **73**, 014014 (2006); **73**, 079903(E) (2006).

[11] T. Barnes, S. Godfrey, and E. S. Swanson, Higher charmonia, Phys. Rev. D **72**, 054026 (2005).

[12] P. G. Ortega, J. Segovia, D. R. Entem, and F. Fernández, Charmonium resonances in the 3.9 GeV/c^2 energy region and the $X(3915)/X(3930)$ puzzle, Phys. Lett. B **778**, 1 (2018).

[13] K. Miyake and Y. Yamaguchi, Hidden-charm tetraquarks in a mixture model: Coupled-channel analysis with $c\bar{c}$ and hadronic molecular components, Phys. Rev. D **112**, 036004 (2025).

[14] S. Uehara *et al.* (Belle Collaboration), Observation of a $\chi c2$ candidate in $\gamma\gamma \to D\bar{D}$ production at BELLE, Phys. Rev. Lett. **96**, 082003 (2006).

[15] B. Aubert *et al.* (*BABAR* Collaboration), Observation of the $\chi_{c2}(2p)$ meson in the reaction $\gamma\gamma \to D\bar{D}$ at *BABAR*, Phys. Rev. D **81**, 092003 (2010).

[16] E. Wang, H.-S. Li, W.-H. Liang, and E. Oset, Analysis of the $\gamma\gamma \to D\bar{D}$ reaction and the $D\bar{D}$ bound state, Phys. Rev. D **103**, 054008 (2021).

[17] O. Deineka, I. Danilkin, and M. Vanderhaeghen, Dispersive analysis of the $\gamma\gamma \to D\bar{D}$ data and the confirmation of the DD bound state, Phys. Lett. B **827**, 136982 (2022).

[18] M. Hoferichter, D. R. Phillips, and C. Schat, Roy-Steiner equations for $\gamma\gamma \to \pi\pi$, Eur. Phys. J. C **71**, 1743 (2011).

[19] L.-Y. Dai and M. R. Pennington, Comprehensive amplitude analysis of $\gamma\gamma \to \pi^+\pi^-, \pi^0\pi^0$ and $\bar{K}K$ below 1.5 GeV, Phys. Rev. D **90**, 036004 (2014).

[20] I. Danilkin and M. Vanderhaeghen, Dispersive analysis of the $\gamma\gamma^* \to \pi\pi$ process, Phys. Lett. B **789**, 366 (2019).
[21] M. Luscher, Two particle states on a torus and their relation to the scattering matrix, Nucl. Phys. **B354**, 531 (1991).
[22] C. h. Kim, C. T. Sachrajda, and S. R. Sharpe, Finite-volume effects for two-hadron states in moving frames, Nucl. Phys. **B727**, 218 (2005).
[23] R. A. Briceno, Two-particle multichannel systems in a finite volume with arbitrary spin, Phys. Rev. D **89**, 074507 (2014).
[24] D. J. Wilson, C. E. Thomas, J. J. Dudek, and R. G. Edwards (Hadron Spectrum Collaboration), Scalar and tensor charmonium resonances in coupled-channel scattering from lattice QCD, Phys. Rev. Lett. **132**, 241901 (2024).
[25] D. J. Wilson, C. E. Thomas, J. J. Dudek, and R. G. Edwards (Hadron Spectrum Collaboration), Charmonium χ_{c0} and χ_{c2} resonances in coupled-channel scattering from lattice QCD, Phys. Rev. D **109**, 114503 (2024).
[26] S. Navas *et al.* (Particle Data Group), Review of particle physics, Phys. Rev. D **110**, 030001 (2024).
[27] S. Prelovsek, S. Collins, D. Mohler, M. Padmanath, and S. Piemonte, Charmonium-like resonances with $J^{PC} = 0^{++}, 2^{++}$ in coupled $D\bar{D}$, $D_s\bar{D}_s$ scattering on the lattice, J. High Energy Phys. 06 (2021) 035.
[28] P.-P. Shi, M. Albaladejo, M.-L. Du, F.-K. Guo, and J. Nieves, P-wave charmonium contribution to hidden-charm states from a reanalysis of lattice QCD data, Phys. Rev. D **111**, 074043 (2025).
[29] R. G. Edwards, B. Joo, and H.-W. Lin, Tuning for three-flavors of anisotropic clover Fermions with stout-link smearing, Phys. Rev. D **78**, 054501 (2008).
[30] H.-W. Lin *et al.* (Hadron Spectrum Collaboration), First results from $2+1$ dynamical quark flavors on an anisotropic lattice: Light-hadron spectroscopy and setting the strange-quark mass, Phys. Rev. D **79**, 034502 (2009).
[31] L. Liu, G. Moir, M. Peardon, S. M. Ryan, C. E. Thomas, P. Vilaseca, J. J. Dudek, R. G. Edwards, B. Joo, and D. G. Richards (Hadron Spectrum Collaboration), Excited and exotic charmonium spectroscopy from lattice QCD, J. High Energy Phys. 07 (2012) 126.
[32] R. G. Edwards, N. Mathur, D. G. Richards, and S. J. Wallace (Hadron Spectrum Collaboration), Flavor structure of the excited baryon spectra from lattice QCD, Phys. Rev. D **87**, 054506 (2013).
[33] J. J. Dudek, R. G. Edwards, M. J. Peardon, D. G. Richards, and C. E. Thomas, Toward the excited meson spectrum of dynamical QCD, Phys. Rev. D **82**, 034508 (2010).
[34] C. E. Thomas, R. G. Edwards, and J. J. Dudek, Helicity operators for mesons in flight on the lattice, Phys. Rev. D **85**, 014507 (2012).
[35] J. J. Dudek, R. G. Edwards, and C. E. Thomas, S and D-wave phase shifts in isospin-2 pi pi scattering from lattice QCD, Phys. Rev. D **86**, 034031 (2012).
[36] M. Peardon, J. Bulava, J. Foley, C. Morningstar, J. Dudek, R. G. Edwards, B. Joo, H.-W. Lin, D. G. Richards, and K. J. Juge (Hadron Spectrum Collaboration), A Novel quark-field creation operator construction for hadronic physics in lattice QCD, Phys. Rev. D **80**, 054506 (2009).
[37] C. Michael, Adjoint sources in lattice gauge theory, Nucl. Phys. **B259**, 58 (1985).
[38] M. Luscher and U. Wolff, How to calculate the elastic scattering matrix in two-dimensional quantum field theories by numerical simulation, Nucl. Phys. **B339**, 222 (1990).
[39] F. G. Ortega-Gama, J. J. Dudek, and R. G. Edwards (Hadron Spectrum Collaboration), Timelike meson form factors beyond the elastic region from lattice QCD, Phys. Rev. D **110**, 094505 (2024).
[40] D. J. Wilson, R. A. Briceno, J. J. Dudek, R. G. Edwards, and C. E. Thomas, Coupled $\pi\pi, K\bar{K}$ scattering in P-wave and the ρ resonance from lattice QCD, Phys. Rev. D **92**, 094502 (2015).
[41] G. K. C. Cheung, C. O'Hara, G. Moir, M. Peardon, S. M. Ryan, C. E. Thomas, and D. Tims (Hadron Spectrum Collaboration), Excited and exotic charmonium, D_s and D meson spectra for two light quark masses from lattice QCD, J. High Energy Phys. 12 (2016) 089.
[42] S. Okubo, Phi meson and unitary symmetry model, Phys. Lett. **5**, 165 (1963).
[43] G. Zweig, An SU(3) model for strong interaction symmetry and its breaking. Version 1, Report No. CERN-TH-401, 1964, 10.17181/CERN-TH-401.
[44] J. Iizuka, Systematics and phenomenology of meson family, Prog. Theor. Phys. Suppl. **37**, 21 (1966).
[45] M. T. Hansen and S. R. Sharpe, Multiple-channel generalization of Lellouch-Luscher formula, Phys. Rev. D **86**, 016007 (2012).
[46] R. A. Briceno and Z. Davoudi, Moving multichannel systems in a finite volume with application to proton-proton fusion, Phys. Rev. D **88**, 094507 (2013).
[47] R. A. Briceno, J. J. Dudek, and R. D. Young, Scattering processes and resonances from lattice QCD, Rev. Mod. Phys. **90**, 025001 (2018).
[48] A. J. Woss, D. J. Wilson, and J. J. Dudek (Hadron Spectrum Collaboration), Efficient solution of the multichannel Lüscher determinant condition through eigenvalue decomposition, Phys. Rev. D **101**, 114505 (2020).
[49] D. J. Wilson, J. J. Dudek, R. G. Edwards, and C. E. Thomas, Resonances in coupled $\pi K, \eta K$ scattering from lattice QCD, Phys. Rev. D **91**, 054008 (2015).
[50] S. Piemonte, S. Collins, D. Mohler, M. Padmanath, and S. Prelovsek, Charmonium resonances with $J^{PC} = 1^{--}$ and 3^{--} from $\bar{D}D$ scattering on the lattice, Phys. Rev. D **100**, 074505 (2019).
[51] M. Bayar, A. Feijoo, and E. Oset, X(3960) seen in $D_s^+ D_s^-$ as the X(3930) state seen in $D + D-$, Phys. Rev. D **107**, 034007 (2023).
[52] D. Guo, J.-Z. Wang, D.-Y. Chen, and X. Liu, Connection between near the $D_s^+ D_s^-$ threshold enhancement in $B^+ \to D_s^+ D_s^- K^+$ and conventional charmonium $\chi_{c0}(2P)$, Phys. Rev. D **106**, 094037 (2022).
[53] E. Wang, W.-H. Liang, and E. Oset, Analysis of the $e^+e^- \to J/\psi D\bar{D}$ reaction close to the threshold concerning claims of a $\chi_{c0}(2P)$ state, Eur. Phys. J. A **57**, 38 (2021).
[54] F.-K. Guo and U.-G. Meissner, Where is the $\chi_{c0}(2P)$?, Phys. Rev. D **86**, 091501 (2012).
[55] R. G. Edwards and B. Joo, The Chroma software system for lattice QCD, Nucl. Phys. B, Proc. Suppl. **140**, 832 (2005).
[56] M. A. Clark, R. Babich, K. Barros, R. C. Brower, and C. Rebbi, Solving Lattice QCD systems of equations using

mixed precision solvers on GPUs, Comput. Phys. Commun. **181**, 1517 (2010).

[57] R. Babich, M. A. Clark, and B. Joo, Parallelizing the QUDA Library for Multi-GPU Calculations in Lattice Quantum Chromodynamics, in *SC 10 (Supercomputing 2010) New Orleans, Louisiana, November 13-19, 2010* (IEEE, Louisiana, USA, 2010), 10.1109/SC.2010.40.

[58] K. Clark, B. Joo, A. Strelchenko, M. Cheng, A. Gambhir, and R. Brower, Accelerating Lattice QCD Multigrid on GPUs Using Fine-grained Parallelization, in *Proceedings of SC 16 (Supercomputing 2016) Salt Lake City, Utah, November 2016* (IEEE Press, 2016), 10.5555/3014904.3014995.

[59] B. Joó, D. Kalamkar, K. Vaidyanathan, M. Smelyanskiy, K. Pamnany, V. Lee, P. Dubey, and W. Watson, Lattice QCD on Intel Xeon Phi^{TM} coprocessors, in *Supercomputing*, Lecture Notes in Computer Science, edited by J. Kunkel, T. Ludwig, and H. Meuer (Springer, Berlin Heidelberg, 2013), Vol. 7905, pp. 40–54.

[60] B. Joó, MG-PROTO: A Multigrid Library for QCD, https://github.com/JeffersonLab/mg_proto/ (2010).

[61] J. C. Osborn, R. Babich, J. Brannick, R. C. Brower, M. A. Clark, S. D. Cohen, and C. Rebbi, Multigrid solver for clover fermions, Proc. Sci. LATTICE2010 (**2010**) 037.

[62] R. Babich, J. Brannick, R. C. Brower, M. A. Clark, T. A. Manteuffel, S. F. McCormick, J. C. Osborn, and C. Rebbi, Adaptive multigrid algorithm for the lattice Wilson-Dirac operator, Phys. Rev. Lett. **105**, 201602 (2010).

[63] J. Chen, R. G. Edwards, and W. Mao, Graph Contractions for Calculating Correlation Functions in Lattice QCD, in *Platform for Advanced Scientific Computing* (Association for Computing Machinery, NY, USA, 2023), 10.1145/3592979.3593409.

[64] S. Prelovsek, E. Ortiz-Pacheco, S. Collins, L. Leskovec, M. Padmanath, and I. Vujmilovic, Doubly heavy tetraquarks from lattice QCD: Incorporating diquark-antidiquark operators and the left-hand cut, Phys. Rev. D **112**, 014507 (2025).

[65] A. Stump and J. R. Green, Position-space sampling for local multiquark operators in lattice QCD using distillation and the importance of tetraquark operators for $T_{cc}(3875)^{+}$, Phys. Rev. D **113**, 034513 (2026).

[66] W. I. Jay and E. T. Neil, Bayesian model averaging for analysis of lattice field theory results, Phys. Rev. D **103**, 114502 (2021).

[67] S. M. Ryan and D. J. Wilson (Hadron Spectrum Collaboration), Excited and exotic bottomonium spectroscopy from lattice QCD, J. High Energy Phys. 02 (2021) 214.

[68] L. Gayer, S. M. Ryan, and D. J. Wilson (Hadron Spectrum Collaboration), Highly excited B, B_s and B_c meson spectroscopy from lattice QCD, J. High Energy Phys. 01 (2025) 123.